



저작자표시-비영리-변경금지 2.0 대한민국

이용자는 아래의 조건을 따르는 경우에 한하여 자유롭게

- 이 저작물을 복제, 배포, 전송, 전시, 공연 및 방송할 수 있습니다.

다음과 같은 조건을 따라야 합니다:



저작자표시. 귀하는 원저작자를 표시하여야 합니다.



비영리. 귀하는 이 저작물을 영리 목적으로 이용할 수 없습니다.



변경금지. 귀하는 이 저작물을 개작, 변형 또는 가공할 수 없습니다.

- 귀하는, 이 저작물의 재이용이나 배포의 경우, 이 저작물에 적용된 이용허락조건을 명확하게 나타내어야 합니다.
- 저작권자로부터 별도의 허가를 받으면 이러한 조건들은 적용되지 않습니다.

저작권법에 따른 이용자의 권리는 위의 내용에 의하여 영향을 받지 않습니다.

이것은 [이용허락규약\(Legal Code\)](#)을 이해하기 쉽게 요약한 것입니다.

[Disclaimer](#)

공학박사학위논문

가연성 기체 혼합물의 비정상 연소
현상과 가압된 용기의 동적 거동 수
치적 해석

Numerical investigations on abnormal combustion
of gaseous mixtures and dynamic responses of
pressurized vessels

2016년 2월

서울대학교 대학원

기계항공공학부

곽민철

Abstract

Numerical investigations on abnormal combustion of gaseous mixtures and dynamic responses of pressurized vessels

Min-cheol Gwak

Department of Mechanical and Aerospace Engineering

The Graduate School

Seoul National University

For the flow analysis of deflagration to detonation transition (DDT), detonation phenomenon involving combustible gas mixtures (C_2H_4 -Air mixture, C_2H_4 - O_2 mixture, H_2 - O_2 mixture, kerosene-air mixture, etc.) and the behavior of metal (copper, beryllium, steel, etc.) confinements during detonation loading, a multi-material treatment is developed for multi-physics shock analysis of gas mixtures and inert metals.

A high-resolution approach including third-order convex ENO for spatial discretization and third-order Runge-Kutta for time advancement is used to simulate the abnormal combustion of gas mixtures and the elasto-plastic behavior of metals. Treatment of material interfaces uses level sets and is fairly simple and robust. Enforcement of jump conditions across the material interface is achieved by applying a ghost-point-populating technique such as

the ghost fluid method (GFM) to interpolate data into extended regions. The time advancement is based on the method of lines, and it enables multi-dimensional calculations without time splitting in addition to allowing efficient implementation of Runge-Kutta schemes at orders higher than two. The physical models include an ideal equation of state (EOS) for combustible gas mixtures, specifically, a Mie-Gruneisen EOS for an elasto-plastic metal with isotropic linear hardening based on the Johnson-Cook model.

Based on numerical approaches, we conduct various investigations. Firstly, DDT triggered by a shock in a straight or multi-bend tube with obstacle geometry is considered. The C_2H_4 -air mixture filled rigid tube with obstacles is considered to understand the effects of complex confinement and initial flame size on DDT. Our calculations show the generation of hot spots by flame and strong shock interactions, and flame propagation is either restrained or accelerated due to wall obstacles for both straight and bent tubes. The effect of initial flame size on DDT in complex confinement geometry is analyzed as well as the effect of hot spot formation on promoting shock-flame interaction, leading to a full detonation. Secondly, we deal with a multi-material numerical investigation on the propagation of C_2H_4 - O_2 mixture and H_2 - O_2 mixture detonation in elasto-plastic metal tubes. The calculated results are validated against the experimental data, which explains the process of generation and subsequent interaction of the expansion wave with the high strain rate deformation of the walls. Finally, to consider realistic wall effects

on the propagating detonation, we perform a numerical simulation on the detonation propagation of kerosene-air mixtures and the perturbations of the detonation field from one elastically vibrating and one thermo-elasto-plastically deforming tube. The detonation loading of the metal tube is validated with experimental cell size, and the burst pressure of copper and steel tubes for varying wall thicknesses and wall temperatures is compared with the theoretical results. The safety aspect of the detonation tube is addressed and the results show that the calculated critical tube thickness with thermal softening included is a better fit with the theoretical value than the calculation without thermal softening. Some of the unseen behaviors of the flow dynamics of a pulsed detonation wave inside a pressure loaded hot tube are reported.

The numerical approaches provide insight into understanding the effects of complex geometry on detonation transition, the influence of distortional tubes on detonation propagation, the dynamic responses of pressurized vessels in terms of the safety issues in accidents related to detonation and the design issues of PDE operated at high temperatures.

***Keywords:* Combustible gas mixture, Abnormal combustion, Deflagration to detonation transition (DDT), Detonation, Elasto-plastic metal, Multi-material treatment**

***Student Number:* 2007-20762**

LIST

ABSTRACT.....	i
LIST.....	iv
LIST OF FIGURES.....	vii
LIST OF TABLES.....	xiv
PREFACE.....	xv
CHAPTER 1	
INTRODUCTION.....	1
CHAPTER 2	
NUMERICAL MODEL.....	7
2.1 Governing equation and constitutive relations	7
2.2 Interface tracking and treatment.....	12
CHAPTER 3	
DDT IN COMPLEX GEOMETRY	18
3.1 Numerical setup.....	18
3.2 Results and discussion.....	21
3.2.1 Validation and grid resolution test	21
3.2.2 Effect of curved wall.....	25

3.2.3 Effect of obstacle size.....	31
3.2.4 Effect of initial flame size.....	37
CHAPTER 4	
DEFORABLE WALL EFFECT ON DETONATION.....	40
4.1 Numerical setup.....	40
4.2 Results and discussion.....	43
4.2.1 Validation and grid resolution test.....	43
4.2.2 Plastic response of metal.....	46
4.2.3 Multi-material problem.....	51
4.2.4 Rigid tube.....	60
4.2.5 Thin-walled tube.....	62
CHAPTER 5	
REALISTIC WALL EFFECTS ON DETONATION.....	67
5.1 Numerical setup.....	67
5.2 Results and discussion.....	69
5.2.1 Validation and grid resolution test	69
5.2.2 Elastic response of metal.....	74
5.2.3 Combined response of detonation loaded elasto- plastic copper and steel tube	82
5.2.4 Perturbed detonations in the elastic vibrating tube...89	

CHAPTER 6

CONCLUSION.....91

REFERENCES.....94

LIST OF FIGURES

Fig. 1.1. Pictures of Explosion accidents such as (a) Explosion of natural gas pipeline in California and (b) Elbow tube rupture at Hamaoka-1, Japan	1
Fig. 3.1. Schematic of (a) bent tube and (b) straight tube, both with varying obstacle size ($h=0$ (smooth), 2.5 (small), and 5 mm (large)). Pressure gauges are located at 1 (64.2 mm), 2 (103.6 mm), 3 (143 mm), 4 (182 mm), and 5 (221.4 mm) from left inlet along centerline.....	20
Fig. 3.2. Pressure history from experiment [35] and calculation of C_2H_4 -air mixture	22
Fig. 3.3. Comparison between detonation transition times from 0.2, 0.1, and 0.05 mm resolutions for $Ma=2.7$	23
Fig. 3.4. Temperature and pressure (in separate window) under $Ma=2.1$ incident shock interacting with an ethylene-air flame in Type-(III) tube. HS and D mean hot spot and detonation, respectively.....	26
Fig. 3.5. Temperature and pressure (in separate window) under $Ma=2.7$ incident shock interacting with an ethylene-air flame in Type-(III) tube....	27
Fig. 3.6. Pressure histories shown by tube types taken at every 500 cycles for $Ma=2.7$ case: Type-(I) Straight no obstacle; Type-(II) Straight with obstacle; Type-(III) Bend no obstacle; Type-(IV) Bend with obstacle.....	29

Fig. 3.7. Straight tube with four obstacles ($h=5$ mm) showing temperature (Kelvin) field. $Ma=2.7$ incident shock accelerated flame of ethylene-air mixture developing into a detonation at time 0.218 ms	31
Fig. 3.8. Comparison of energy release rate for different tube types under $Ma=2.7$ incident shock.....	32
Fig. 3.9. Comparison of detonation transition distance in Type-(III, IV) with obstacle size ($h = 0, 2.5,$ and 5 mm) and varying incident shock strength.....	33
Fig. 3.10. GO/No GO map on incident shock strength and obstacle size of the bent tube.....	33
Fig. 3.11. Comparison of chemical energy release rate in Type-(III, IV) under $Ma=2.1$	34
Fig. 3.12. Obstacle size comparison. Temperature and pressure (in separate window) under $Ma=2.5$ incident shock interacting with an ethylene-air flame in Type-(IV) with obstacles ($h=2.5$ mm: (a)-(b), $h=5$ mm: (c)-(d))..	36
Fig. 3.13. Comparison of detonation transition (a) time and (b) distance in Type-(III) for different initial flame size and varying incident shock strength tested.....	37
Fig. 3.14. Initial flame size comparison, temperature and pressure (in separate window) under $Ma=2.5$ incident shock interacting with an ethylene-air flame in Type-(III) for different initial flame size r_f ((a), (b): detonation; (c): fast deflagration at 0.241 ms).....	38

Fig. 4.1. Schematic of deformation of copper tube by H ₂ -O ₂ detonation loading (unit: mm).....	40
Fig. 4.2. Pressure profiles of four different mesh sizes (0.1, 0.05, 0.02, and 0.01 mm)	43
Fig. 4.3. (a) Pressure profiles of H ₂ -O ₂ mixture detonation and reflected shock and (b) various C-J pressure of experiment [37] and simulation.....	44
Fig. 4.4. Pressure, species, reaction rate and temperature near detonation front in a stoichiometric H ₂ -O ₂ mixture.....	45
Fig. 4.5. Comparisons of theoretical exact solution, reference [38], and our calculation result at 200 μs.....	46
Fig. 4.6. Mesh resolution test using particle velocity profile.....	47
Fig. 4.7. Schematic of 2D cylindrical calculation setup for Taylor problem.....	48
Fig. 4.8. Histories of the values of total, kinetic, and internal energy density under Taylor impact.....	48
Fig. 4.9. Comparison between experimental data [44] and numerical results of copper rod shape.....	49
Fig. 4.10. Comparison between analytical [34] and numerical solution in Shock tube problems using Eq. (4.1)	51
Fig. 4.11. Comparison between analytical [34] and numerical solution in Shock tube problems using Eq. (4.2)	52
Fig. 4.12. Schematic of underwater explosion (unit: mm)	53

Fig. 4.13. Pressure contours and interfaces at 15.3 and 31.7 ms.....	54
Fig. 4.14. Comparison between the Ref. [41] (hollow) and ours (filled symbols)	55
Fig. 4.15. Schematic of elasto-plastic deformation of steel tube by C ₂ H ₄ -O ₂ mixture detonation (unit: mm)	57
Fig. 4.16. Pressure history from experiment [20] and calculation of C ₂ H ₄ -air mixture.....	58
Fig. 4.17. Comparisons of experiment [20] and numerical results of residual plastic strain.....	59
Fig. 4.18. Snapshots of density [unit: kg/m ³] in a rigid tube. Arrows indicate the propagation direction.....	60
Fig. 4.19. Pressure histories of an ideal (1D model) and rigid tube (2D cylindrical model)	61
Fig. 4.20. Snapshots of density [unit: kg/m ³] in the thin-walled tube (0.12 mm thickness tube)	62
Fig. 4.21. Snapshots of density [unit: kg/m ³] in the thin-walled tube (0.16 mm thickness tube)	64
Fig. 4.22. Comparison between the rigid (0.2 mm thickness) and the thin-walled (0.12 mm thickness) tubes using (a) pressure histories, (b) density fields of each tube at 6.5 μs, and (c) effective plastic strain fields in tube at 8 μs.....	65
Fig. 4.23. Comparison between the rigid (0.2 mm thickness) and the thin-	

walled (0.16 mm thickness) tubes using (a) pressure histories, (b) density fields of each tube at 15.5 μ s, (c) effective plastic strain fields in tube at 17 μ s.....	66
Fig. 5.1. Schematic of kerosene-air mixture detonation in elasto-plastic tube (unit: mm).....	68
Fig. 5.2. Mesh resolution test for kerosene-air mixture detonation (1/15, 1/50, and 1/100 mm).....	70
Fig. 5.3. Pressure history in solid line and temperature in dashed shown at 10 μ s.....	70
Fig. 5.4. Schematic of shock tube simulation for kerosene-air mixture detonation at various initial gas pressures.....	71
Fig. 5.5. Shadowgraph of calculated detonation cell structure of kerosene-air mixture at 1 bar initial pressure.....	72
Fig. 5.6. Detonation cell width of kerosene-air mixture in comparison....	73
Fig. 5.7. Schematic of elastic vibration.....	74
Fig. 5.8. Initial input (Y-axis velocity) condition ($A=100$)	75
Fig. 5.9. Comparison between FEM result based on Ref. [43] and ours using history of y-axis velocity at center point.....	76
Fig. 5.10. Snapshots of velocity magnitude (unit: m/s) field inside of beryllium	76
Fig. 5.11. Comparison between with and without gas mixture using y-axis velocity histories at center point.....	77

Fig. 5.12. Histories of y-axis velocity at center point in various initial velocity magnitude.....	78
Fig. 5.13. Snapshots of deviatoric stress, S_{rr} field inside of plate and pressure field in gas mixture.....	79
Fig. 5.14. Pressure histories at numerical gauges P1, P2, P3, and P4 in gas mixture.....	81
Fig. 5.15. Snapshots of density [unit: kg/m^3] in (a): $T_w = 433 \text{ K}$, $t = 0.2 \text{ mm}$, (b): $T_w = 433 \text{ K}$, $t = 0.15 \text{ mm}$, and (c) $T_w = 973 \text{ K}$, $t = 0.15 \text{ mm}$, all of which taken at $11.5 \mu\text{s}$ without thermal softening.....	82
Fig. 5.16. Effect of thermal softening plotted with effective plastic strains at cold (433 K) and hot (973 K) wall temperature conditions.....	83
Fig. 5.17 Snapshots of density [unit: kg/m^3] in two cases of (a) no thermal softening and (b) with thermal softening under $T_w = 773 \text{ K}$ and $t = 0.25 \text{ mm}$ copper tube.....	84
Fig. 5.18. Snapshots of impedance fields [unit: $\text{kg}/\text{m}^2\text{s}$] in comparison between (a) with thermal softening and (b) no thermal softening $T_w = 950 \text{ K}$ and $t = 0.1 \text{ mm}$ 304 SS tube.....	85
Fig. 5.19. DAF versus velocity of varying (a) copper and (b) 304 SS tubes thicknesses.....	86
Fig. 5.20. The calculated (symbol) and theoretical (solid line) critical thickness plotted against heated wall temperature for (a) Copper and (b) 304 SS.....	88

Fig. 5.21. Pressure profiles of detonation in rigid and elastic vibrating tubes
.....89

Fig. 5.22. Snapshots of density [unit: kg/m^3] at times 8 and 14 μs for (a)
rigid wall and (b) elastic vibrating tubes.....90

LIST OF TABLES

Table 3.1. Initial condition and material properties of C ₂ H ₄ -air mixture.....	21
Table 3.2. Comparison between experiment and numerical results.....	23
Table 4.1. Initial condition and material properties of H ₂ -O ₂ mixture.....	41
Table 4.2 Initial condition and material properties of copper.....	41
Table 4.3. Comparison between experimental data and simulation results....	50
Table 4.4. Initial condition of hot air, ambient air, and water.....	53
Table 4.5. Initial condition and material properties of C ₂ H ₄ -O ₂ mixture.....	56
Table 4.6. Initial condition and material properties of steel (304 SS).....	56
Table 5.1. Initial condition and material properties of kerosene-air mixture..	69
Table 5.2. Initial condition and material properties of Beryllium.....	75

PREFACE

This thesis is based on the following publications and manuscripts

Chapter 3

Min-cheol Gwak and Jack J. Yoh, "Effect of multi-bend geometry on deflagration to detonation transition of a hydrocarbon-air mixture in tubes," *International Journal of Hydrogen Energy*, Vol. 38, pp. 11446-11457, 2013

Chapter 4

Ki-Hong Kim, Min-cheol Gwak, and Jack J. Yoh, "An Enhanced Particle Reseeding Algorithm for the Hybrid Particle Level Set Method in Compressible Flows," *Journal of Scientific Computing*, Vol. 65, pp. 431–453, 2015

Min-cheol Gwak, Younghun Lee, Ki-hong Kim, and Jack J. Yoh, "Deformable wall effects on the detonation of combustible gas mixture in a thin-walled tube," *International Journal of Hydrogen Energy*, Vol. 40, pp. 3006-3014, 2015

Chapter 5

Younghun Lee, Min-cheol Gwak, and Jack J. Yoh, "Numerical investigation of kerosene-based pulse detonation loading on the metal tubes," *Journal of Propulsion and Power*, accepted

The chapters are reproduced with permission of the co-authors and the publishers.

CHAPTER 1

INTRODUCTION

Abnormal combustion such as detonation wave is a reactive shock wave supported by the rapid chemical reaction that results in a sudden increase of pressure and temperature, leading to an extreme thermodynamic state within a very short time. When it is accompanied by the structural deformation or a failure, such internal explosion and detonation in structures can raise a major safety concern. For instance, the internal explosion of fuel transporting pipe lines may trigger pipe rupture and a catastrophic disaster [1, 2].



(a)



(b)

Fig. 1.1. Pictures of Explosion accidents such as (a) Explosion of natural gas pipeline in California and (b) Elbow tube rupture at Hamaoka-1, Japan

If one properly understands the mechanism of structure deformation (or failure) induced by the interaction between the gaseous detonation and the confinements, aforementioned personnel and material losses by explosion may be minimized. Also, in aircraft and space propulsion systems, as a pulse detonation engine (PDE) is a highly efficient engine which uses the high potential energy caused by high pressure and temperature of an abnormal combustion, it has been continuously developed [3-10].

For these reasons, deflagration to detonation transition (DDT) and detonation has maintained continued interest in the combustion community for experimental, theoretical, and numerical investigations [11-13].

The DDT is an extremely complicated process involving deflagrations, shocks, reflected shocks, boundary layers, and their interactions. In the literature, there are known mechanisms of DDT as addressed in recent years. The Richtmyer-Meshkov (RM) instability resulting from repeated shockeflame interactions and bifurcated structure formed by reflected shock and boundary layer interaction generates turbulent flames. The turbulent flames create conditions in a nearby unreacted gas, which leads to generation of hot spots for developing a detonation through the Zel'dovich gradient mechanism [14]. The temperature gradient triggers DDT at localized hot spots that are formed ahead of the flame front. Both modes of burning can be expressed by a single-step chemical reaction which satisfies the characteristic length and time of deflagration and detonation [11]. Another view on the DDT

mechanism suggests that a temperature gradient mechanism is unnecessary, and that a multi-step chemical reaction must be considered. The pressure amplified by the positive feedback between the pressure rise and the enhanced reaction in the front edge of the flame would lead to preheat zone formation and flame acceleration, responsible for such transition to detonation [13].

These rather distinct views on the mechanism have something in common: the interaction between a strong shock wave, and the critical role of flame acceleration leading to DDT. In most laboratory experiments, the onset of DDT is believed to originate somewhere within the strange shock structure enhanced by the multiple interactions of the shock, reflected shock, and flame. This shock-flame interaction can be strengthened when encountered by complex geometries such as walls, obstacles, and curves within pipes due to multiple reflections of shocks and expanded flame surfaces. In view of the shock and flame interaction being the main cause of DDT, researchers have looked at such phenomena in pipes in order to gain better understanding of geometrical factors responsible for DDT. In Refs. [11] and [12], comprehensive reviews on the gaseous DDT induced from the shock and flame interaction in straight tube are discussed. A consideration of the effect of obstacles is made in Refs. [12], where the enhancement of shock and flame interactions, instabilities, and flame and vortex interaction in obstacle wakes brings about the growth of the flame surface, the energy-release rate, and the intensity of the shock. Also the change in DDT triggering time and position

due to the obstacle spacing and size was shown. With an emphasis on the effect of curves within pipes [15, 16] showed how the curvature and tube diameter in a U-bend tube change the detonation propagation characteristics. Although these studies showed valuable information on a fully developed detonation in tubes, the transition study from a deflagration to a detonation subject to complex confinement geometries has not been addressed until now. So we investigate DDT in a multi-bend geometry with obstacles for comparison to a straight geometry to understand the factors responsible for triggering flame acceleration and termination. Since the initial flame size is indicative of flame surface condition [11], different flame size in two-dimensional tube geometry is also considered to provide insight into the transition dynamics of gaseous deflagrations.

Studies on the developed detonation in tubes of varying thickness have been performed by the researchers for building and utilizing propulsion and power systems such as PDE [17-19]. These studies are focused on the internal detonation flow subjected to a rigid boundary wall. When tubes can no longer persist yielding due to a detonative loading, it is then plastically deformed and subsequent response influences the internal flow, likely generating compression or expansion waves. Previously, experimental and numerical studies of deformed or fractured tubes under detonation loading have been conducted [20-24]. These studies accomplished quantitative measurements and numerical predictions of elasto-plastic behaviors of tubes under such

loadings. So, we consider in detail the dynamics of elasto-plastic response of tubes of varying thicknesses. Despite several reported attempts known to simulate explosively deformed tube due to a condensed phase detonation [25, 26], nothing has been done for elasto-plastic response of the metal tube subjected to a gas mixture detonation. Thus, the gaseous detonation and its interaction with the thin-walled metal tubes under multi-material treatment are studied, and the obtained results are validated against the experimental data and the theory.

Also the operation of PDE follows in sequence the detonation ignition, propagation, and reactant refilling. In the detonation propagation stage, gas temperature can exceed 3000K during a few microseconds of instant wave propagation. The tube temperature rise during this time is insignificant, and heat transfer at the tube wall cannot cause tube deformation. However, PDE is operated with multiple pulses of detonation propagation, whose frequency is 10~30 Hz, as the tube is constantly exposed to a harsh thermal conditions, and the tube temperature is rise to near 1000 K [9]. The increased tube temperature leads to mechanical properties of the tube in PDE, and the high temperature provides an easy condition for the tube to damage. Also, in real phenomenon, the PDE could be elastically vibrated at its various natural frequencies under internal and external stimulations. Previously, many researchers have treated detonated tube like fixed tube [4-6, 22] when detonation is simulated in the tube except for consideration of an elastic

vibration which may not be dominate factor of detonation propagation. However the elastic vibration induces minutely oscillated wall which ingenerates perturbations of flame during detonation propagation.

The contents of this thesis are arranged as follows. In chapter 2, numerical model is introduced including governing equations consisting of mass, momentum, and energy conservation, and formulation of ‘tuned’ one step chemical reaction of combustible gas mixture is proposed. Also constitutive relations to close the system including evolution of stress to describe the behavior of solid are shown. In chapter 3, to investigate change of detonation transition time/distance by geometry effect, we deal with DDT of ethylene-air mixture in complex geometry including curved wall, obstacle size, and initial flame size. In chapter 4, we confirm deformable wall effect on detonation utilizing behaviors of thin-walled copper tube under detonation of hydrogen-oxygen mixture. In chapter 5, realistic wall effects induced by thermal softening and elastic vibrating tube on detonation in PDE system are examined. Finally, conclusions are given in chapter 6.

CHAPTER 2

NUMERICAL MODEL AND SETUP

2.1 Governing equation and constitutive relations

The two-dimensional, conservative hyperbolic equation for reactive compressible flow consists of the conservative laws of mass, momentum, energy, and species in an axisymmetric cylindrical ($\alpha=1$, r- and z-axis) and rectangular ($\alpha=0$, x- and y-axis) coordinate given as

$$\frac{\partial U}{\partial t} + \frac{\partial G}{\partial r} + \frac{\partial F}{\partial z} + H = 0 \quad (2.1)$$

$$U = (\rho, \rho u_r, \rho u_z, \rho e, \rho Y_i)^T$$

$$E = (\rho u_r, \rho u_r^2 + P, \rho u_r u_z, u_r (\rho e + P), \rho Y_i u_r)^T$$

$$F = (\rho u_z, \rho u_r u_z, \rho u_z^2 + P, u_z (\rho e + P), \rho Y_i u_z)^T \quad (2.2)$$

$$H = \left(\eta \frac{\rho u_r}{r}, \eta \frac{\rho u_r^2}{r}, \eta \frac{\rho u_r u_z}{r}, \eta \frac{u_r (\rho e + p)}{r} - \rho Q_i \dot{w}_i, -\rho \dot{w}_i \right)^T$$

where ρ , u_r , u_z , P , s_{ij} , e , Q_i , \dot{w} , and Y_i are density, r-axis velocity, z-axis velocity, pressure, deviatoric stress, total energy density, chemical energy release, chemical reaction rate, and mass fraction of the reactant mixture, respectively.

Also $\dot{w}_i \equiv \partial Y_i / \partial t|_{chem} = A \rho Y \exp(-E_a / (RT))$, reaction rate is described by the experimentally tuned first-order Arrhenius kinetics. It chosen based on its

feasibility to accurately resolve key length and time scales involved in the deflagration to detonation transition. Using theoretical equations based on adiabatic flame temperature and CJ detonation velocity, we determine heat capacity ratio and chemical energy release to be determined. Also, pre-exponential factor is set by solving the energy equation in laminar flame condition such as laminar flame velocity and thickness and by using half-reaction thickness based on ZND theory and the given initial conditions [11].

For metal, the following conservative laws of mass, momentum, and energy in an axisymmetric cylindrical ($\alpha=1$, r- and z-axis) and rectangular ($\alpha=0$, x- and y-axis) coordinate are used. Also the deviatoric stress tensor, S_{ij} fields are calculated together with the evolution equations based on a Hooke's law and the plasticity flow theory for high strain rate deformation are shown in Eq. (2.3). Where, T , α , λ , G , $\Omega_{ij}=(\partial u_i/\partial x_j-\partial u_j/\partial x_i)/2$, $\Sigma=(\partial u/\partial r+u/r+\partial v/\partial z)/3$, D_{ij} , β , and D^P_{ij} are current temperature, thermal expansion coefficient, Lamé's first parameter, shear modulus, spin tensor, volume strain rate, strain rate tensor, Taylor-Quinney parameter, and plastic strain rate, respectively.

$$\begin{aligned}
 U &= (\rho, \rho u_r, \rho u_z, \rho e, S_r, S_z, S_{rz})^T \\
 E &= (\rho u_r, \rho u_r^2 + P, \rho u_r u_z, u_r (\rho e + P), S_r u_r, S_z u_r, S_{rz} u_r)^T \\
 F &= (\rho u_z, \rho u_r u_z, \rho u_z^2 + P, u_z (\rho e + P), S_r u_z, S_z u_z, S_{rz} u_z)^T
 \end{aligned} \tag{2.3}$$

$$H = \begin{pmatrix} \alpha \frac{\rho u_r}{r} \\ \alpha \frac{\rho u_r^2}{r} - \frac{\partial S_{rr}}{\partial r} - \frac{\partial S_{rz}}{\partial z} \\ \alpha \left(\frac{\rho u_r u_z}{r} - \frac{S_{rz}}{r} \right) - \frac{\partial S_{rz}}{\partial r} - \frac{\partial S_{zz}}{\partial z} \\ \alpha \left(\frac{u_r(\rho e + p) - (u_r S_{rr} + u_z S_{rz})}{r} \right) - \frac{\partial (u_r S_{rz} + u_z S_{zz})}{\partial z} - \frac{\partial (u_r S_{rr} + u_z S_{rz})}{\partial r} \\ + \left(\alpha T (3\lambda + 2G)(D_{rr} + D_{zz}) + \beta \sqrt{\text{tr}(D_{ij}^p D_{ij}^p) \text{tr}(S_{ij} S_{ij})} \right) \\ - 2S_{rz} \Omega_{rz} - S_{rr} \left(\frac{\partial u_r}{\partial r} + \frac{\partial u_z}{\partial z} \right) - 2G \left(\frac{\partial u_r}{\partial r} - \Sigma - D_{rr}^p \right) \\ 2S_{rz} \Omega_{rz} - S_{zz} \left(\frac{\partial u_r}{\partial r} + \frac{\partial u_z}{\partial z} \right) - 2G \left(\frac{\partial u_z}{\partial z} - \Sigma - D_{zz}^p \right) \\ - \Omega_{rz} (S_{zz} - S_{rr}) - S_{rz} \left(\frac{\partial u_r}{\partial r} + \frac{\partial u_z}{\partial z} \right) - 2G \left(\frac{1}{2} \left(\frac{\partial u_r}{\partial z} + \frac{\partial u_z}{\partial r} \right) - D_{rr}^p \right) \end{pmatrix}$$

The plastic strain rate tensor is derived by Eq. (2.4) which satisfies the physical constraint using the radial return algorithm [27, 28].

$$D_{ij}^p = \Lambda N_{ij} = \frac{d}{dt} \left(\frac{\bar{\sigma} - \sigma_y}{\sqrt{6G} \left(1 + \frac{h}{3G} \right)} \right) \frac{S_{ij}}{\sqrt{S_{kl} S_{kl}}} \quad (2.4)$$

where, Λ , $\bar{\sigma} = \sqrt{3(S_{rr}^2 + S_{zz}^2 + S_{rr}S_{zz} + S_{rz}^2)}$, and h are positive parameter called the consistency parameter, effective plastic strain, and hardening coefficient, respectively.

The pressure of the combustible gas mixture is calculated by the ideal equation of state, $P(\rho, T) = \rho RT$ with R being the universal gas constant or $P(e, \nu) = (\gamma - 1)e/\nu$ with ν , the ratio of specific heats. As for the elasto-plastic metal, the Mie-Gruneisen equation of state Eq. (2.5), and the rate-dependent Johnson-Cook strength model, Eq. (2.6) are used:

$$p(\rho, e) = \rho_0 \Gamma_0 e + \begin{cases} \frac{\rho_0 c_0^2 \varphi}{(1-s\varphi)^2} \left[1 - \frac{\Gamma_0}{2} \varphi \right] & \text{if } \rho \geq \rho_0 \\ c_0^2 (\rho - \rho_0) & \text{otherwise} \end{cases} \quad (2.5)$$

$$\sigma_Y = \left(\sigma_{Y,0} + A (\bar{\varepsilon}^P)^n \right) \left(1 + B \ln \left(\frac{\dot{\bar{\varepsilon}}^P}{\dot{\varepsilon}_0} \right) \right) \left(1 - \left(\frac{T - T_0}{T_m - T_0} \right)^m \right) \quad (2.6)$$

where Γ_0 , s , c_0 , A , B , n and m are material constants, and ρ_0 , T_m , T_0 , and $\dot{\bar{\varepsilon}}^P = \sqrt{2/3} \Lambda$ are initial density, melting temperature, ambient temperature, and effective plastic strain rate, respectively. The unknown scalar parameter Λ means time differentiation of Γ whose closed form is expressed like Eq. (2.7).

$$\Gamma = \int_{t_0}^{t_1} \Lambda dt = \frac{\sqrt{S_{ij,tr} : S_{ij,tr}} - \sqrt{\frac{2}{3}} \sigma_v^0}{2G(1 + \frac{h}{3G})} = \sqrt{\frac{2}{3}} \frac{\bar{\sigma}_{tr} - \sigma_v^0}{2G(1 + \frac{h}{3G})} = \frac{\bar{\sigma}_{tr} - \sigma_v^0}{\sqrt{6}G(1 + \frac{h}{3G})} \quad (2.7)$$

During the numerical simulation, the control of the time step increment follows time constraints that the code automatically chooses as appropriate time step based on numerical properties of the dynamic simulation. In two dimensions, the CFL time step is calculated from Eq. (2.8)

$$\Delta t_{CFL} = CFL \times \min \left\{ \frac{\Delta r}{\max |d\bar{E} / d\bar{U}|}, \frac{\Delta z}{\max |d\bar{F} / d\bar{U}|} \right\} \quad (2.8)$$

where CFL is the Courant number, $\max |d\bar{E} / d\bar{U}|$ and $\max |d\bar{F} / d\bar{U}|$ are the largest eigenvalues (in absolute sense) of the Jacobians of \bar{E} and \bar{F} which are the convective flux vectors in r- and z- direction.

The governing equations are solved by a 3rd Runge-Kutta (RK) and the Convex ENO method in the temporal and spatial discretization, respectively.

2.2 Interface tracking and treatment

To track the interface between the different materials, namely the combustible gas and the metal tube, a hybrid particle level set (HPLS) method based on a ghost fluid method (GFM) is applied.

A level-set method [29-32] provides a simple way to track a multi-material interface that may separate a combustible gaseous mixture from a container (tube), for example. The sharp discontinuity of state variables across the interface is handled using the level sets. The level-set equation in two dimensions below tracks the location of the contact surface represented by the zero-level contour $\phi(x,y)=0$,

$$\frac{\partial \phi}{\partial t} + u_i \cdot \nabla \phi = 0 \quad (2.9)$$

Initially, ϕ is taken as a signed normal distance function to the interface. The material interface evolves with local material velocity. The material velocity on either side of the interface provides the velocity extension that is used for advection of ϕ in the level-set domain. The level-set function ϕ is taken positive outside of material and negative inside, and ϕ is initialized to be a signed normal distance from the material interface.

The re-initialization of level-set contours is a necessary procedure for making sure that no steep gradient enters into the smooth level-set field of distance function, ϕ . This requires solving of the following equation until a steady state is reached:

$$\phi_\tau + S(\phi)(|\nabla\phi| - 1) = 0, \quad S = \frac{\phi}{\sqrt{\phi^2 + (1 - |\nabla\phi|)^2 \Delta x^2}} \quad (2.10)$$

where the smeared sign function is defined S . Then Eq. (2.10) is solved by the Godunov's scheme like Eq. (2.11)

$$\begin{aligned} \phi^{n+1} = \phi^n - \frac{\Delta\tau}{\Delta x} S^+ & \left(\sqrt{\max[(a^+)^2, (b^-)^2] + \min[(c^+)^2, (d^-)^2]} - 1 \right) \\ & - \frac{\Delta\tau}{\Delta x} S^- \left(\sqrt{\max[(a^-)^2, (b^+)^2] + \min[(c^-)^2, (d^+)^2]} - 1 \right) \end{aligned} \quad (2.11)$$

where $a^\pm, b^\pm, c^\pm, d^\pm$ are the Godunov fluxes, and the monotonicity of Eq. (2.14) is enforced by restricting the time step as follows $|S| \leq 0.5\Delta\tau / \Delta x$.

Geometrical quantities can be calculated from the level set function, including the unit normal, \bar{n} and the curvature, κ like Eq. (2.12)

$$\bar{n} = \frac{\nabla\phi}{|\nabla\phi|}, \quad \kappa = \nabla \cdot \bar{n} = \nabla \cdot \left(\frac{\nabla\phi}{|\nabla\phi|} \right) \quad (2.12)$$

To improve the interface tracking, we condition a hybrid particle level set method which consists of level set function and massless marker particles. Two sets of massless marker particles are placed near the interface with one set, the positive particles, in the $\phi > 0$ region and the other set, the negative particles, in the $\phi \leq 0$ region. It is unnecessary to place particles far from the interface since the sign of the level set function easily identifies these regions. This greatly reduces the number of particles needed in a given simulation. The particles are advected with the evolution Eq. (2.13).

$$\frac{d\bar{x}_p}{dt} = \bar{u}(\bar{x}_p) \quad (2.13)$$

where \bar{x}_p is the position of the particle and $\bar{u}(\bar{x}_p)$ is its velocity. The particle velocities are interpolated from the velocities on the underlying grid. This trilinear interpolation limits the particle evolution to second-order accuracy. A third-order accurate TVD Runge–Kutta method is used to evolve the particle positions forward in time. The particles are used to both track characteristic information and reconstruct the interface in regions where the level set method has failed to accurately preserve mass.

For the purpose of interface reconstruction, a sphere of radius r_p is centered at each particle location, \bar{x}_p . The radius of each particle is bounded by minimum and maximum values based upon the grid spacing. In two dimension, maximum and minimum radii are decided by $r_{\min} = 0.1 \min(\Delta x, \Delta y)$ and $r_{\max} = 0.5 \max(\Delta x, \Delta y)$.

Two sets (positive and negative) of particles are randomly placed within a band across the interface. A given number (N_p) of particles of each sign are placed in each node, for instance, 16 particles in two dimension were used in this study. An “attraction” technique is used to relocate the particles to the corresponding side (of the same sign) of the interface. The above process is the so-called particle seeding operation. Each particle stores its position and radius, which is used to perform error correction to the level set function. The radius of the particles is determined by Eq. (2.14)

$$r_p = \begin{cases} r_{\max} & \text{if } s_p \phi(\bar{x}_p) > r_{\max} \\ s_p \phi(\bar{x}_p) & \text{if } r_{\min} \leq s_p \phi(\bar{x}_p) \leq r_{\max} \\ r_{\min} & \text{if } s_p \phi(\bar{x}_p) < r_{\min} \end{cases} \quad (2.14)$$

where s_p is the sign of the particle, set to determination of Eq. (2.15)

$$s_p = \begin{cases} 1 & \text{if } \phi(\bar{x}_p) > 0 \\ -1 & \text{if } \phi(\bar{x}_p) < 0 \end{cases} \quad (2.15)$$

In each time step, the level set function is advected for a whole RK cycle first, then the positions of the particles are updated using the third-order TVD RK scheme. In the well-resolved regions, the level set solution is adequately accurate and the particles just follow the motion of the interface as defined by the grid-based level set function. But in the under-resolved regions, particles may drift across the interface due to excessive regularization of the level set solution. When a particle escapes the interface by more than its radius, it will be used to perform error correction on the interface. The level set value given by an escaped particle with a radius r and a position vector x is defined as follows Eqs. (2.16) and (2.17) for an escaped positive and negative particle p , respectively.

$$\phi_p(x) = \begin{cases} s_p (r_p - |x - x_p|) & \text{if } \phi(x) < 0 \\ s_p (r_p + |x - x_p|) & \text{if } \phi(x) > 0 \end{cases} \quad (2.16)$$

$$\phi_p(x) = \begin{cases} s_p (r_p - |x - x_p|) & \text{if } \phi(x) > 0 \\ s_p (r_p + |x - x_p|) & \text{if } \phi(x) < 0 \end{cases} \quad (2.17)$$

Error correction is performed using the grid-based ϕ^+ and ϕ^- , which

represent the positive and negative level set regions(with reduced errors) generated by the escaped positive and negative particles, respectively. For each positive escaped particle, ϕ_p is found for each corner of the node that contains the particle. The value for each corner sets to $\phi^+ = \max(\phi_p, \phi^+)$.

For each negative escaped particle, ϕ_p is similarly defined for each corner of the node that contains the particle. The value for each corner sets to $\phi^- = \max(\phi_p, \phi^-)$.

Note that both ϕ^+ and ϕ^- in the above two equations are initialized with ϕ . The level set function is then reconstructed using ϕ^+ and ϕ^- by choosing the value with minimum magnitude at each grid node based on Eq. (2.18). Error corrections are performed both after the level set advection and reinitialization.

$$\phi = \begin{cases} \phi^+ & \text{if } |\phi^+| \leq |\phi^-| \\ \phi^- & \text{if } |\phi^+| > |\phi^-| \end{cases} \quad (2.18)$$

To sum up, the procedure of the operations in the original method is advect the level set function and update the positions of the particles, correct level set function using the escaped particles, reinitialize the level set function, correct the level set function using the particles again, and finally adjust the particle radii. When an interface involves severe deformations, some regions may lack a sufficient number of particles whereas a large amount of particles may pile up in some other regions. It is necessary to perform particle reseeded

operations, i.e., periodically readapt particle distributions near the interface. The interested reader is referred to Ref. [33] for more detailed description of the particle level set method.

The zero level of level set marks the location of the interface, while the positive values correspond to one material and the negative values correspond to the other. The discretization of the level set function in Eq. (2.10) can be done independent of the two sets of Euler equations. This will be done with the help of ghost nodes which play role of boundary condition of each material. Multi-material treatment is to define a ghost node at every point in the computational domain. In this way, each grid point will contain the mass, momentum, and energy for the real fluid that exists at that point (according to the sign of the level set function) and a ghost mass, momentum, and energy for the other fluid that does not really exist at the point (it is on the other side of the interface). Once the ghost nodes are defined, we can use standard methods, to update the Euler equations at every grid point for both materials. The description of GFM is discussed in Ref. [25, 34].

CHAPTER 3

DDT IN COMPLEX GEOMETRY [17]

3.1 Numerical setup

We performed DDT simulation of a stoichiometric ethylene-air mixture subject to a variety of incident shock intensities at Mach numbers ranging from 1.9 to 2.7. The effects of curved wall and obstacles are considered with bent tube and three different obstacle sizes, and the different initial flame size is also tested.

We make comparison of four different geometrical confinements by their types:

Type-(I) Straight tube with no obstacle

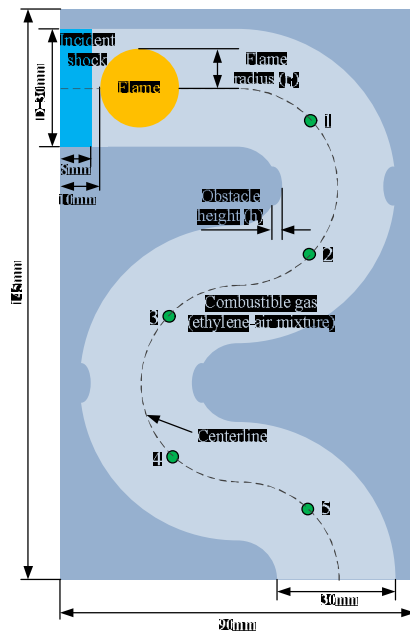
Type-(II) Straight tube with obstacles

Type-(III) Bent tube with no obstacle

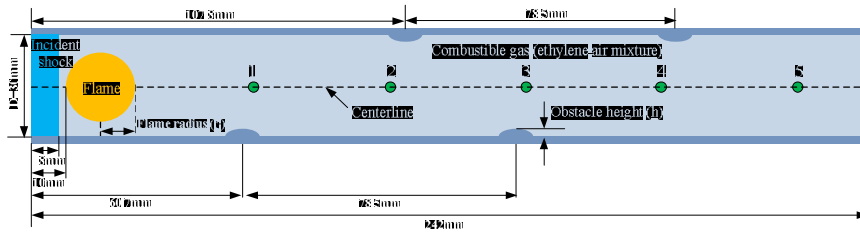
Type-(IV) Bent tube with obstacles

The complex confinement effects at the onset of DDT are investigated through various combinations of wall turning in the flow downstream, varying size of obstacle within tube, and initial flame size. We configured the bends with obstacles to confirm the effects of curved wall and obstacle size. The numerical domain of the bent tube is 90 mm by 145 mm, with entire tube length being 242 mm based on the centerline length of an 'equivalent' straight

tube (see Fig. 3.1). The straight tube with obstacles is a 242 mm by 30 mm in dimension with no-slip wall condition, using four obstacles positioned at 60.7, 107.8, 139.2 and 186.5 mm. Obstacles of the bent tube are also positioned at the same 4 locations along the wall curvature of a total running length of 242 mm. The incident shock is initially placed 8 mm from the left inlet. A uniform flow is assumed in the post-shock state between the left boundary and the incident shock. The center of a circular flame is initially located at 20 mm from the left, and its initial diameter is 20 mm. The initial flame is assumed to have a discontinuity, where the adiabatic flame conditions (temperature, 2625 K and density, 0.0177 kg/m^3) are separated from the surrounding ambient conditions.



(a) Bent tube – Type-(III, IV)



(b) Straight tube – Type–(I, II)

Fig. 3.1. Schematic of (a) bent tube and (b) straight tube, both with varying obstacle size ($h=0$ (smooth), 2.5 (small), and 5 mm (large)). Pressure gauges are located at 1 (64.2 mm), 2 (103.6 mm), 3 (143 mm), 4 (182 mm), and 5 (221.4 mm) from left inlet along centerline.

In a bent region, the outer and inner radiuses are 40 mm and 10 mm, respectively. We considered 3 different obstacle sizes (height of $h = 0$ (smooth), 2.5 (small obstacle), and 5 mm (large obstacle)), and tested three different initial flame sizes (radiuses of 9, 10, and 11 mm) in the tube. In our model, zero gradient inflow/outflow boundary conditions are applied at inlet and exit in order to prevent any interference with rarefaction or shock reflection on the shock-flame interaction. For comparison of the pressure variation with a straight tube, we use five pressure gauges placed at equidistance from each other along the center axis as shown in Fig. 3.1.

3.2 Results and discussion

3.2.1. Validation and grid resolution test

For simulation of abnormal combustion of C₂H₄-air mixture, using 2D cylindrical reactive compressible Navier-Stokes equations with ‘tuned’ 1 step chemical reaction with ideal gas EOS, we use the initial conditions and material parameters are listed in Table 3.1.

Table 3.1. Initial condition and material properties of C₂H₄-air mixture

Parameter	C ₂ H ₄ -air mixture
Initial density, ρ_0	1.58 kg/m ³
Initial pressure, P_0	1.33x10 ⁵ Pa
Initial temperature, T_0	293 K
Specific heat ratio, γ	1.15
Molecular weight, M_w	29x10 ⁻³ kg/mol
Pre-exponential factor, A	3.2x10 ⁸ m ³ /(kg·s)
Activation energy, E_a	35.351RT ₀ J/mol
Chemical heat release, Q	48.824RT ₀ /M _w J/kg
C-J detonation pressure	12 P ₀
C-J detonation velocity	1870 m/s

The simulation indicates shock-induced ethylene-air experiment in a straight tube without the obstacle based on Ref [35]. Figure 3.2 shows a pressure history from the experiment as compared to our calculation.

Calculated pressure represents peak pressures sampled in the center of tube whereas the experiment is pressure taken near the wall. Comparison is in good agreement in terms of maximum pressure near 1.2 MPa, overall decreasing

tendency, and tail pressure being approximately 0.4 MPa. Noticeable fluctuations are observed in both cases where complex wall reflections of shocks are presumed responsible. Additionally, our calculation suggests that velocity and pressure of the strange wave are approximately 932 m/s and 0.52 MPa, respectively.

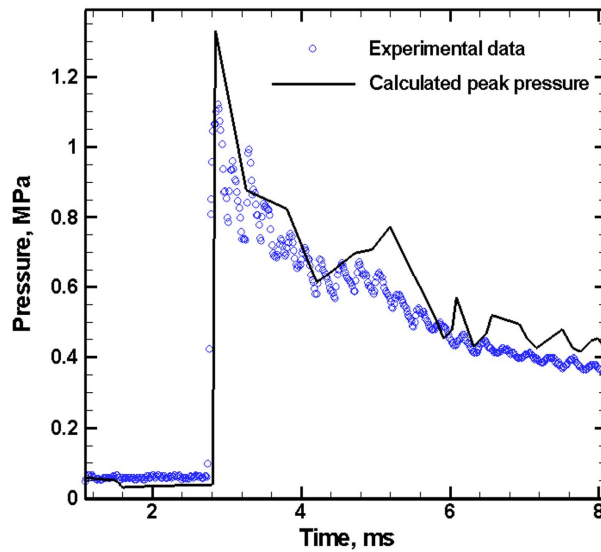


Fig. 3.2. Pressure history from experiment [35] and calculation of C_2H_4 -air mixture

Table 3.2 shows a comparison of the velocity and pressure of strange wave versus detonation from the reference, suggesting a strong agreement between experiment and calculation.

Table 3.2. Comparison between experiment and numerical results

		Experiment [10]	Numerical results
Strange wave	Pressure, MPa	0.53	0.52
	Velocity, m/s	~ 850	932
Detonation	Pressure, MPa	1.2	1.33
	Velocity, m/s	1870	2076

The reaction zone thickness is carefully resolved by requiring a mesh size to be 0.1 mm. Three levels of grid refinements (0.2, 0.1, and 0.05 mm) were tested for checking grid independence, and 0.1 mm was chosen to be optimal for hotspot identification in the flame zone. This resolution corresponds to approximately 10 computational cells in the ethylene-air mixture's laminar flame thickness of about 0.96 mm.

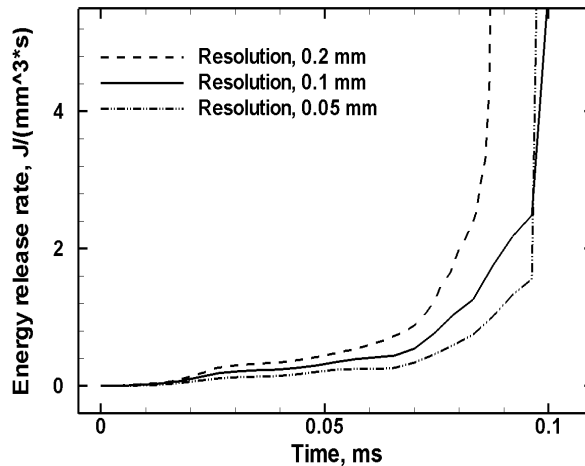


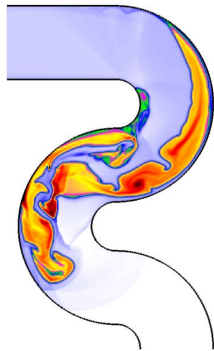
Fig. 3.3. Comparison between detonation transition times from 0.2, 0.1, and 0.05 mm resolutions for $Ma=2.7$

Figure 3.3 shows a history of the energy release rate ($J/(mm^3K)$) in accordance with three mesh resolutions for the case of $Ma=2.7$ bent tube with large obstacle. The detonation transition time and position for both resolutions 0.1 mm and 0.05 mm are 0.101 ms and at the corner of first obstacle, respectively.

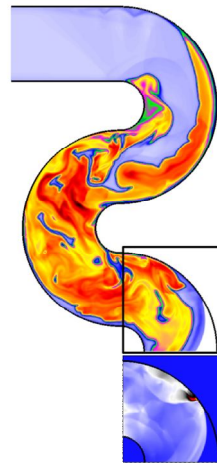
3.2.2. Effect of curved wall

The effect of curved wall on DDT is considered by making comparison of a multi bend to a straight tube. In general, the interaction between boundary layer, shock, and flame gives rise to hot spot formation, which can trigger a detonation transition. In a straight tube long enough to clear the minimum distance needed for a DDT for an ethylene-air mixture, the detonation transition will always occur in the case of a strong shock intensity (roughly $Ma > 2.5$). However, we used a shorter test tube (242 mm) in which no transition can occur regardless of the incident shock strength, while we observed DDT in a bent tube subject to a weak shock intensity at $Ma = 2.1$.

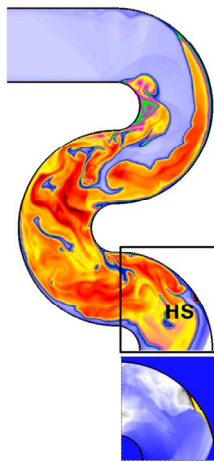
The temperature and pressure fields in a smooth bent tube subject to $Ma = 2.1$ are shown in Fig. 3.4. The flame is distorted and expanded by a shock and flame interaction due to presence of the curved walls (see Fig. 3.4(a)). During this process, the shock is strengthened forming a strange wave packet. This enhanced shock strength generates hot spots near the surface of the curved wall. In both Figs. 3.4(b) and (c), the strange wave propagates downstream, and it is noticeably reinforced; the wave intensity is strengthened while propagating along the curved wall. Eventually, a hot spot is generated at a specific location on the wall at 0.363 ms. Hence, detonation propagates outwards toward the surrounding from this point onwards (see Fig. 3.4(d)).



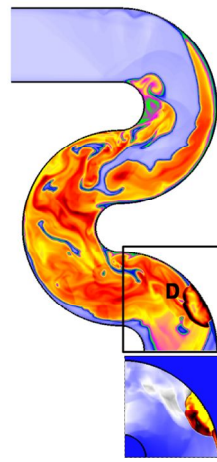
(a) Flame acceleration, 0.3 ms



(b) Formation of strong shock wave, 0.359 ms



(c) Hot spot formation, 0.363 ms

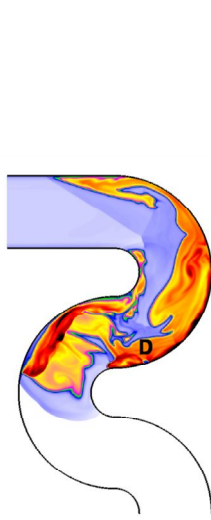


(d) Detonation propagation, 0.367 ms

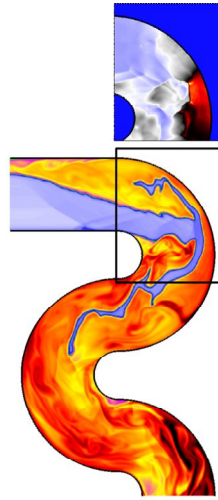
Temperature (Kelvin): 0 800 1600 2400 3200

Pressure (MPa): 0 0.5 1

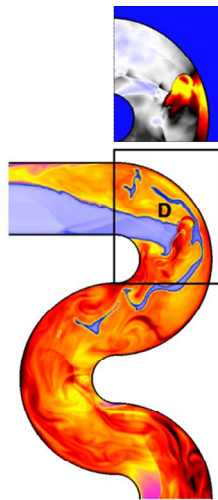
Fig. 3.4. Temperature and pressure (in separate window) under $Ma=2.1$ incident shock interacting with an ethylene-air flame in Type-(III) tube. HS and D mean hot spot and detonation, respectively



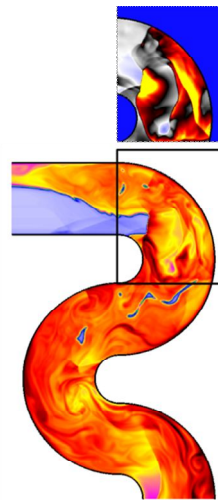
(a) Flame acceleration, 0.3 ms



(b) Formation of strong shock wave, 0.359 ms



(c) Hot spot formation, 0.363 ms



(d) Detonation propagation, 0.367 ms

Temperature (Kelvin):  0 800 1600 2400 3200


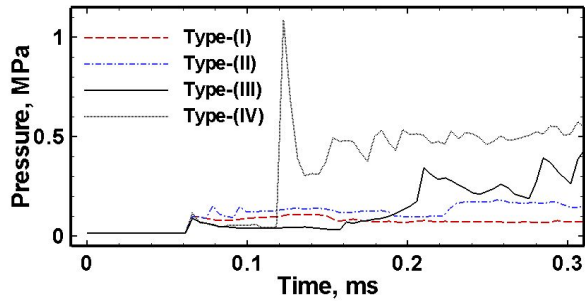
Pressure (MPa):  0 0.5 1

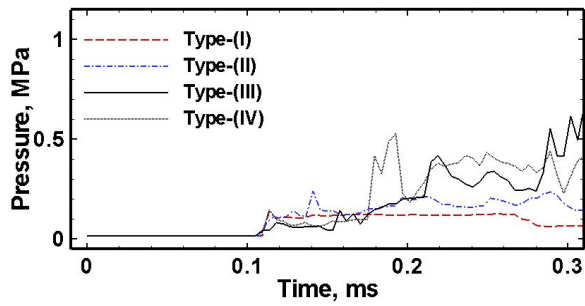
Fig. 3.5. Temperature and pressure (in separate window) under $Ma=2.7$ incident shock interacting with an ethylene-air flame in Type-(III) tube

Next, we consider a strong shock intensity at $Ma=2.7$, as shown in temperature and pressure fields of Fig. 3.5. The first detonation transition appears near the second curved wall at 0.179 ms (see Fig. 3.5(a)). However, this flame does not propagate upstream because of opposite walls and the absence of reactants. In Fig. 3.5(b), a detonation wave propagates upstream along the wall near the flame. Then, the wave makes contact with two flame tips and repeatedly interacts with flames and the curved wall. Through this process, a hot spot is formed between two flame tips, and a second detonation is triggered from this point (see Figs. 3.5(c) and (d)). In order to confirm the curved wall effect, we compare this observation to a straight tube under the same shock intensity at $Ma=2.7$.

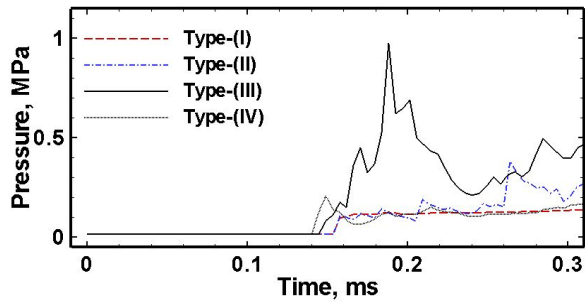
Figure 3.6 shows pressure histories of all 4 tubes as tested at 5 gauge locations. For starter, we look at tubes with no obstacles which correspond to lines (I) and (III). By inspection, bent tube-(III) pressure fluctuates and is significantly increased due to the propagation of a strong shock wave and detonation. The peak pressure also does not exceed CJ detonation pressure for (III) since reactants burn out before detonation occurs. However, the emerging strange wave is confirmed as the pressure ranges from 0.4 to 1.1 MPa at time 0.293 ms. At locations different from gauging points, detonation pressures ranging from 0.6 to 2.7 MPa (CJ detonation pressure being 1.2 MPa) are shown for bent tube-(III) in Figs. 3.6(c)-(d).



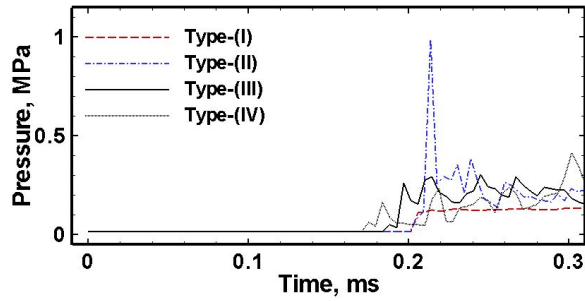
(a) Gauge 1 (64.2 mm)



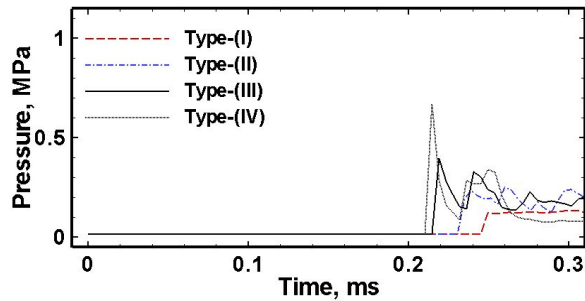
(b) Gauge 2 (103.6 mm)



(c) Gauge 3 (143 mm)



(d) Gauge 4 (182 mm)



(e) Gauge 5 (221.4 mm)

Fig. 3.6. Pressure histories shown by tube types taken at every 500 cycles for $Ma=2.7$ case: Type-(I) Straight no obstacle; Type-(II) Straight with obstacle; Type-(III) Bend no obstacle; Type-(IV) Bend with obstacle

The pressure fluctuation is due to shock disturbances and release of the chemical energy of reactant. The pressure increases beyond 2 MPa in the reactant-rich flow condition, whereas the magnitude of pressure increase is below 1 MPa in the reactant-deficient condition. Pressure signals for straight tube-(I) remains smooth throughout, showing no sign of DDT.

3.2.3. Effect of obstacle size

Figure 3.7 shows temperature field of Type-(II), a straight tube with large obstacle ($h=5$ mm), using an incident shock wave, $Ma=2.7$. In the figure, at 0.205 ms, a detonation occurs in front of a fourth obstacle. This suggests that detonation transition time and distance of straight tube with obstacle are 0.205 ms and 181.11 mm, which are much shorter than the straight tube case.

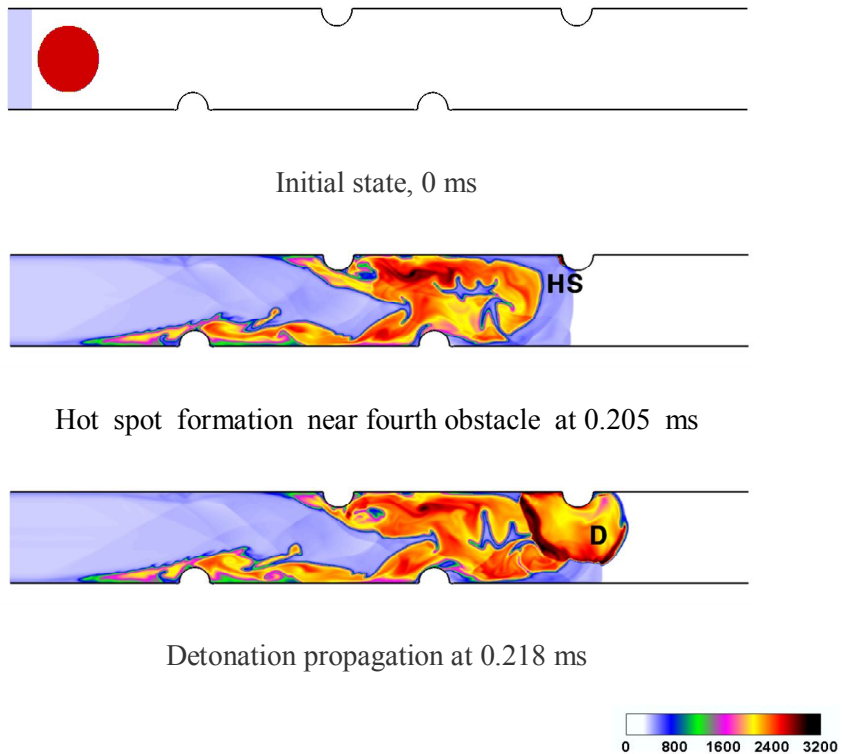


Fig. 3.7. Straight tube with four obstacles ($h=5$ mm) showing temperature (Kelvin) field. $Ma=2.7$ incident shock accelerated flame of ethylene-air mixture developing into a detonation at time 0.218 ms.

However, these are longer than Type-(IV), bent tube with obstacles (0.1 ms, 81.65 mm) and Type-(III) without obstacles (0.162 ms, 119.32 mm) based on a jump in the chemical energy release rate (see Fig. 3.8). Therefore the curved wall is an effective means of a detonation transition, and thus the combination of curved wall with obstacles or Type-(IV) is an optimal choice.

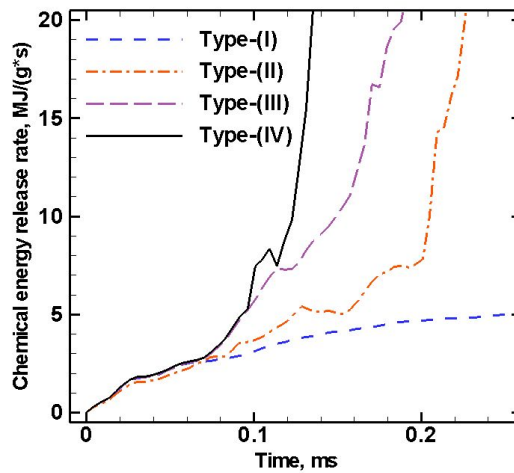


Fig. 3.8. Comparison of energy release rate for different tube types under $Ma=2.7$ incident shock

Figure 3.9 shows the transition distance of Type-(III) and (IV) with different obstacle sizes ($h = 0, 2.5, \text{ and } 5 \text{ mm}$) and varying incident shock strength. The detonation distance is decreased along the increasing obstacle size and incident shock intensity.

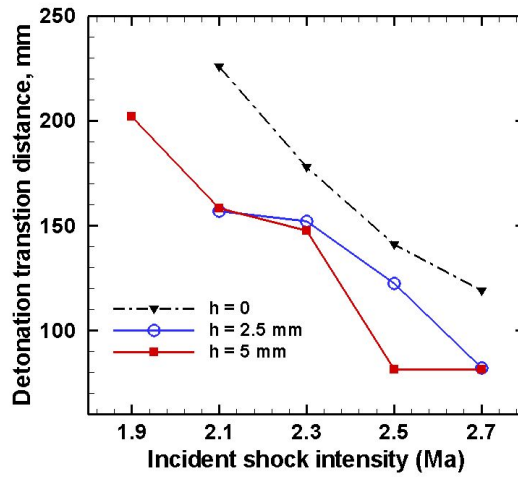


Fig. 3.9. Comparison of detonation transition distance in Type-(III, IV) with obstacle size ($h = 0, 2.5,$ and 5 mm) and varying incident shock strength

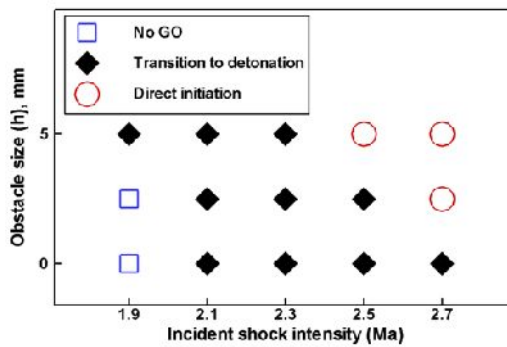


Fig. 3.10. GO/No GO map on incident shock strength and obstacle size of the bent tube

This tendency shown in Fig. 3.10 also presents a GO/No GO region on the plane of incident shock strength versus obstacle size. The obstacle effect in

Type-(IV) is checked through a comparison with the chemical heat release rates of smooth Type-(III).

Figure 3.11 shows that the detonation transition in the large obstacle case (at 0.324 ms) is faster than the smooth case (at 0.363 ms) as seen in the first peak appearing time. In the large obstacle case, the peak value near 20 MJ/(g·s) is reached from 0.29-0.36 ms and at 0.486 ms, corresponding to a first and second detonation. Here, the chemical energy release rate is approximately 20 MJ/g·s when detonation transition occurs, which is the same for both smooth and small obstacle cases. In the smooth case, the peak is shown at 0.363 ms upon detonation, after which the chemical heat release rate is sustained at almost half of the peak value near 10 MJ/(g·s)

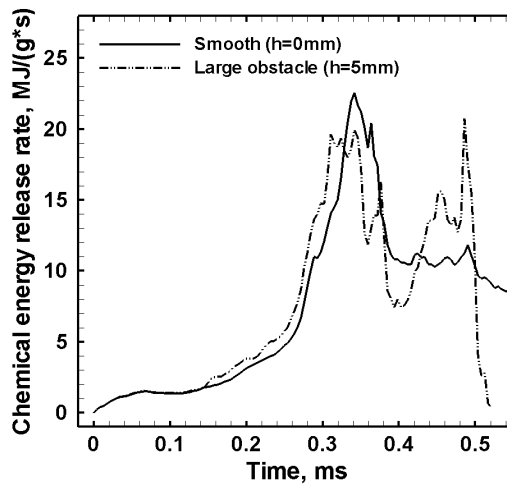
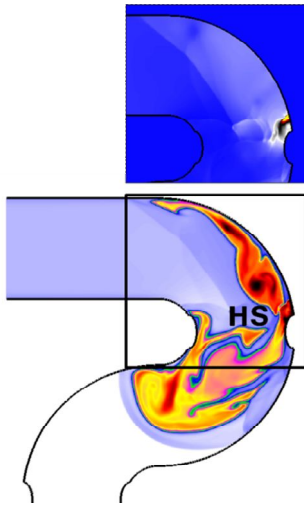
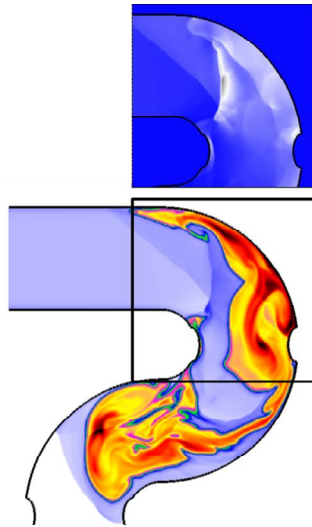


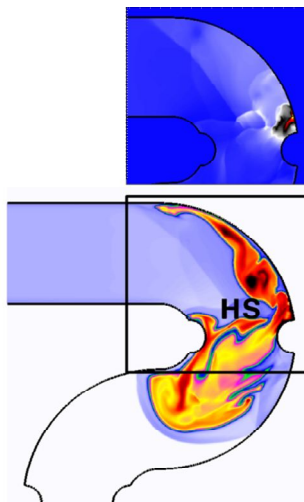
Fig. 3.11. Comparison of chemical energy release rate in Type-(III, IV) under Ma=2.1



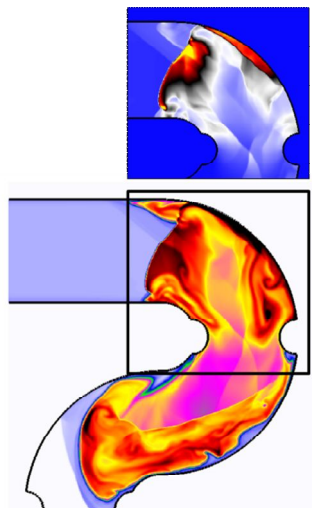
(a) Hot spot formation, 0.144ms



(b) Fast deflagration propagation,
0.175 ms



(c) Hot spot formation, 0.14 ms



(d) Detonation propagation, 0.175 ms

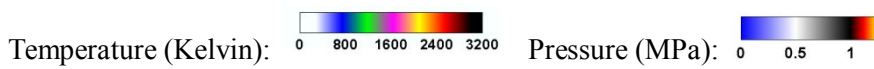


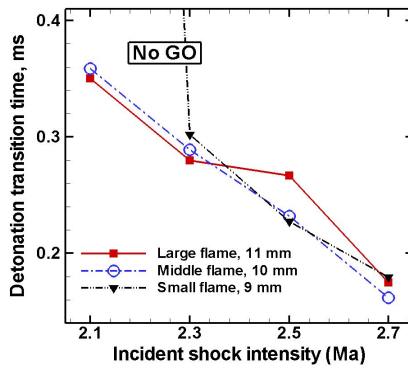
Fig. 3.12. Obstacle size comparison. Temperature and pressure (in separate window) under $Ma=2.5$ incident shock interacting with an ethylene-air flame in Type-(IV) with obstacles ($h=2.5$ mm: (a)-(b), $h=5$ mm: (c)-(d))

Figure 3.12 shows flame propagation details of small and large obstacle cases at $Ma=2.5$. In comparison, the formation of hot spots and direct initiation from these hot spots in each case are observed. In the small obstacle case, a hot spot did not directly initiate a detonation (see Fig. 3.12(a), (b)), due to insufficient reactants at a pressure of 0.9 MPa and at temperature of 600 K. In the large obstacle case, however, hot spot can initiate a direct detonation (see Fig. 3.12(c), (d)) because of a sufficiently high pressure of 1 MPa and temperature of 900 K. Hot spots of both cases are observed at nearly identical locations with similar intensity.

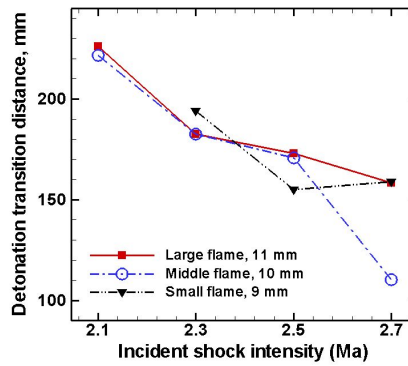
Nevertheless, direct initiation differed due to the flame shape, intensity of the shock reflection, and shock-flame interactions, which are influenced by the differences in confinement geometry.

3.2.4. Effect of flame size

To confirm the effect of initial flame size, we consider three different flame radii ($r_f = 9, 10, \text{ and } 11 \text{ mm}$). Figure 3.13 shows the first detonation transition time and distance for each case.

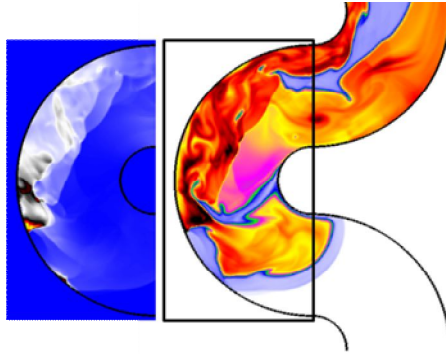


(a)

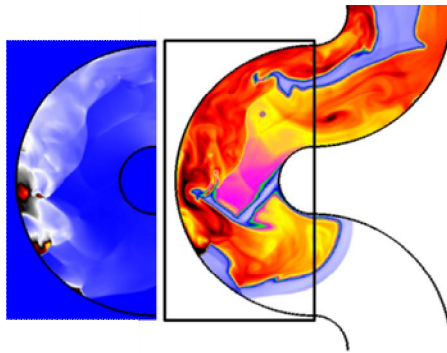


(b)

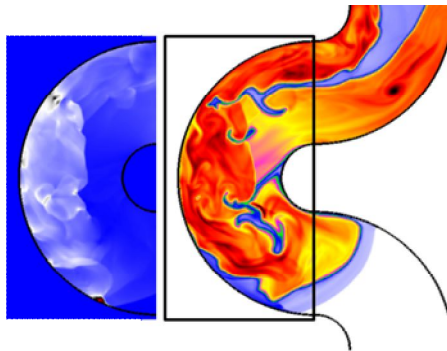
Fig. 3.13. Comparison of detonation transition (a) time and (b) distance in Type-(III) for different initial flame size and varying incident shock strength tested



(a) $r_f = 9$ mm



(b) $r_f = 10$ mm



(c) $r_f = 11$ mm



Temperature (Kelvin):  Pressure (MPa): 

Fig. 3.14. Initial flame size comparison, temperature and pressure (in separate window) under $Ma=2.5$ incident shock interacting with an ethylene-air flame in Type-(III) for different initial flame size r_f ((a), (b): detonation; (c): fast deflagration at 0.241 ms)

The time to detonation is decreased regardless of flame size for increasing shock intensity. The initial flame size either accelerates or delays the transition to a detonation under different incident shock intensities. In the weak incident shock condition (below Mach 2.3), the detonation transition in large flame is slightly faster because of the initially wider flame surface that induces acceleration of the shock and the flame. The small flame results in delayed transition because of low temperature (750 K), pressure (0.82 MPa), and reactant fraction at $Ma=2.3$. The detonation transition in a small incident flame does not occur at $Ma=2.1$. However, in the strong incident shock condition ($Ma=2.5$), the larger initial flame leads to a delayed transition due to the absence of reactants in the regions of complex confinement, such that the detonation transition in large flame is slow.

In Figs. 3.14(a) and (b), pressure field shows detonation transition at 0.241 ms, which is different from Fig. 3.14(c). This noticeable effect of initial flame size is shown to depend closely on the surrounding geometry.

CHAPTER 4

DEFORABLE WALL EFFECT ON DETONATION

[6, 33]

4.1 Numerical setup

We consider a stoichiometric H_2-O_2 mixture that fills a copper tube having the different thicknesses ($t= 0.12, 0.16,$ and 0.2 mm) subjected to a detonation loading.

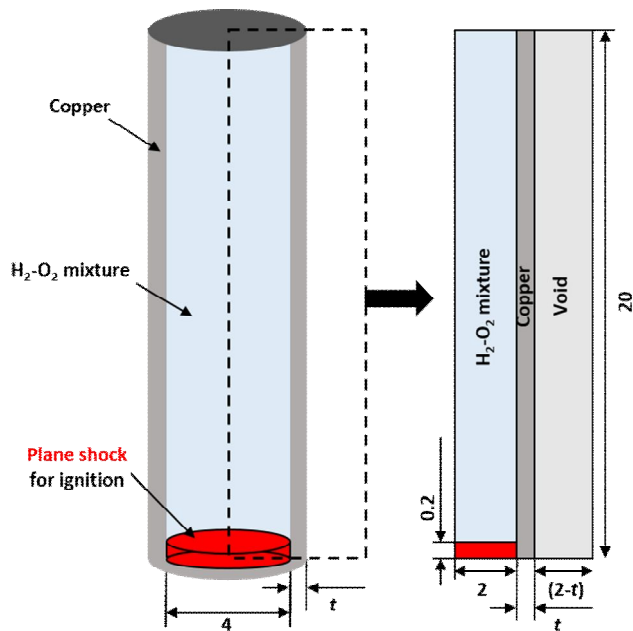


Fig. 4.1. Schematic of deformation of copper tube by H_2-O_2 detonation loading (unit: mm)

Table 4.1 shows the initial conditions and the mechanical and chemical parameters of the gaseous mixture. And Table 4.2 summarizes the initial parameters of copper.

Table 4.1. Initial condition and material properties of H₂-O₂ mixture

Parameter	H ₂ -O ₂ mixture
Initial density, ρ_0	0.493 kg/m ³
Initial pressure, P_0	1.001x10 ⁵ Pa
Initial temperature, T_0	293 K
Specific heat ratio, γ	1.333
Molecular weight, M_w	11.8x10 ⁻³ kg/mol
Pre-exponential factor, A	7x10 ⁸ m ³ /(kg s)
Activation energy, E_a	69036 J/mol
Chemical heat release, Q	4.867x10 ⁶ J/kg
C-J detonation pressure	17.3 P_0
C-J detonation velocity	2845 m/s

Table 4.2. Initial condition and material properties of copper

Parameter	Copper [6]
Initial density, ρ_0	8930 kg/m ³
Shear modulus, G	45 GPa
Yield stress, Y	90 MPa
Gruneisen coefficient, Γ_0	2.0
Normal sound speed, c_0	3940 m/s
S	1.49
Thermal conductivity, k	400 W/(m-K)
Poisson's ratio, ν	0.35
Melting temperature, T_m	1358 K

The 2D cylindrical domain is shown in Fig. 4.1, where section of a detonation tube ($r_i = 2$ mm; $L = 20$ mm) is considered with the three different tube thicknesses. The boundary conditions of top, left, right, and bottom are wall, symmetric, zero gradient, and extrapolated conditions ($X_{boundary} = 0.95X_l + 0.05X_\theta$), respectively. For detonation initiation, a CJ condition is initially assigned near the bottom.

4.2 Results and discussion

4.2.1. Validation and grid resolution test

Making use of 1D reactive compressible Euler equations with ‘tuned’ 1 step chemical reaction with ideal gas EOS, we validate the detonation of $\text{H}_2\text{-O}_2$ mixture.

Firstly, we consider a mesh resolution test by varying the mesh size in order to fulfill the mesh resolution requirement. Figure 4.2 shows pressure profiles of four different mesh sizes 0.1, 0.05, 0.02, and 0.01 mm in detonations of $\text{H}_2\text{-O}_2$ mixture. Here, 0.02 and 0.01 mm resolutions show an identical detonation structure in terms of its position and strength of a von Neumann spike and CJ pressure.

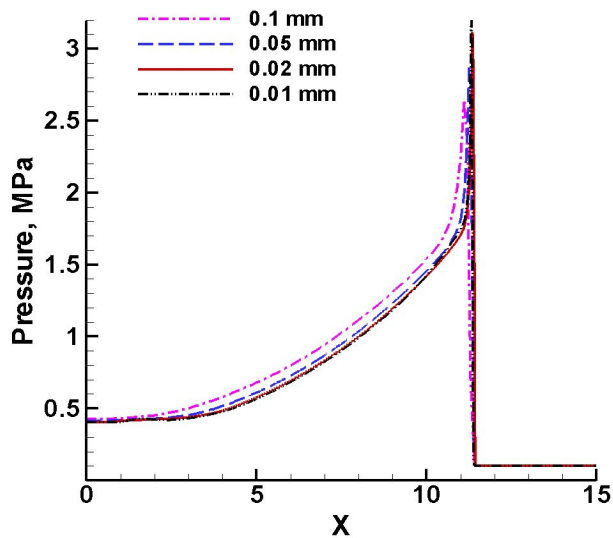
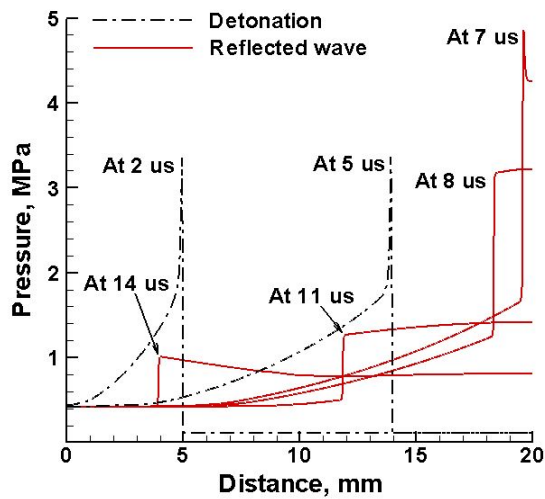


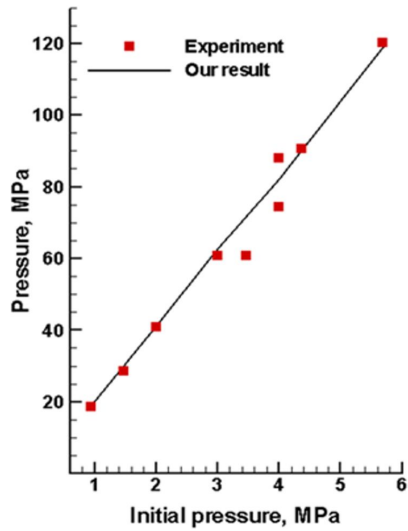
Fig. 4.2. Pressure profiles of four different mesh sizes (0.1, 0.05, 0.02, and 0.01 mm)

Accordingly, we use 0.02 mm resolution which is reasonable to reproduce the pressure and detonation velocity, although the mesh size is coarser than those used by Ref. [36]. Figure 4.3 shows (a) propagation of detonation and reflected shock profiles at initial pressure 1 bare and (b) pressure profiles of H₂-O₂ mixture model for various initial pressures. In these figure, CJ pressure is proportional to the initial pressure in both numerical and experimental data [37].

And Fig. 4.4 shows profiles of pressure, species, reaction rate and temperature near detonation front in H₂-O₂ mixture under initial pressure, 0.101 MPa. Here, the peak pressure, CJ pressure, and CJ temperature are 3.38 MPa, 1.89 MPa and 3060 K, respectively, all of which are in good agreement with the experimental data.



(a)



(b)

Fig. 4.3. (a) Pressure profiles of H_2-O_2 mixture detonation and reflected shock and (b) various C-J pressure of experiment [37] and simulation

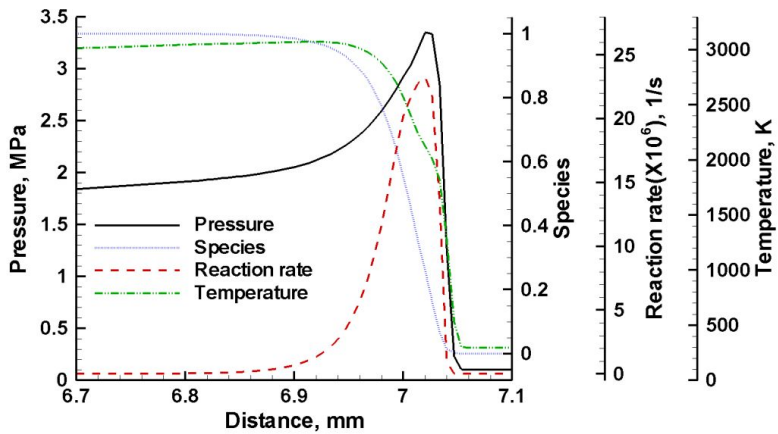


Fig. 4.4. Pressure, species, reaction rate and temperature near detonation front in a stoichiometric H_2-O_2 mixture

4.2.2. Plastic response of metal

Firstly, we consider simple impact problem which is a variant of the example considered in Ref. [38]. In this fictitious 1D problem, a copper (Cu) rod, which is 1 m in length is impacted at the $r = 0$ with constant particle velocity, 40 m/s.

The compression of the copper rod generates an elastic precursor and a plastic wave. To conform these waves, it is required to capture the elastic precursor and plastic wave, waveforms, and the speed of the wave.

The purpose of this example is to demonstrate proper mesh resolution and establish the accuracy of the proposed our numerical approach. Based on 1.25 mm resolution, our numerical results, reference results, and exact solutions [38] are displayed in Fig. 4.5 which shows the plots for pressure at 200 μ s.

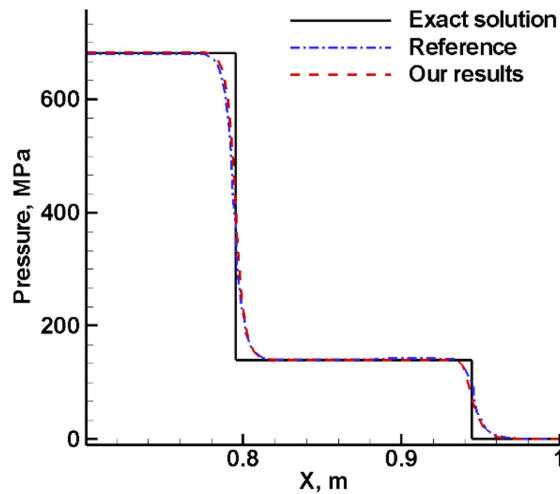


Fig. 4.5. Comparisons of theoretical exact solution, reference [38], and our calculation result at 200 μ s

As evident from the figure, the results from the current calculations are in agreement with the reference results and exact solutions. Figure 4.6 shows the dependency of our numerical solution with grid refinement which indicates that the profile of elastic and plastic waves become sharper with refinement. Here, 0.3125 and 0.15625 mm resolutions show a nearly identical shape of waves. Accordingly, below the 0.3125 mm mesh size is reasonable to reproduce an elastic precursor and a plastic wave. And this mesh size quite larger than requisite mesh size for simulation of abnormal combustion. So mesh size of gaseous mixture determines criterion of decision in proper mesh size of multi-material simulation.

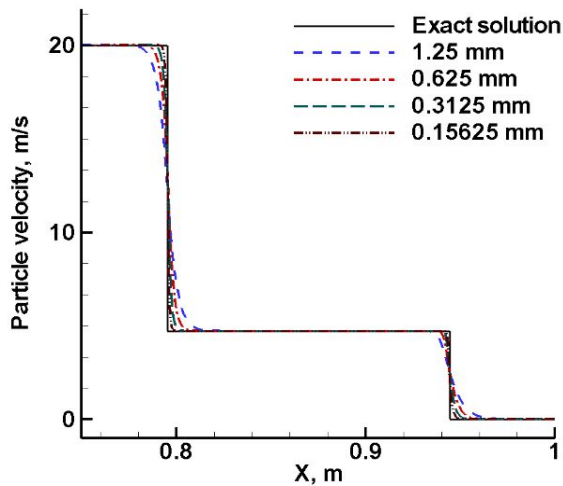


Fig. 4.6. Mesh resolution test using particle velocity profile

As benchmarking problem of plastic deformation which is a normal collision of a cylindrical copper rod with a rigid wall [39], the Taylor impact

problem is considered. Figure 4.7 shows the schematic of the Taylor impact problem. Axisymmetric cylindrical copper rod (57.1 mm X 3.2 mm) is located in calculation domain (58 mm X 8.5 mm). The top, right, left, and bottom boundary conditions are zero gradient, wall, zero gradient, and axisymmetric conditions, respectively. Impact of rod is described by prescribing an initial particle velocity which is 189 m/s.

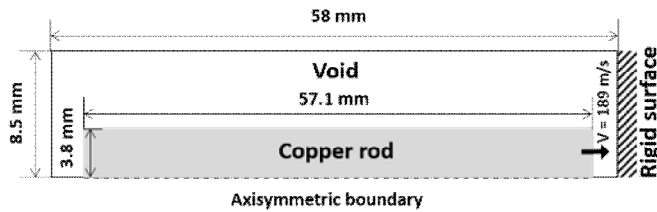


Fig. 4.7. Schematic of 2D cylindrical calculation setup for Taylor problem

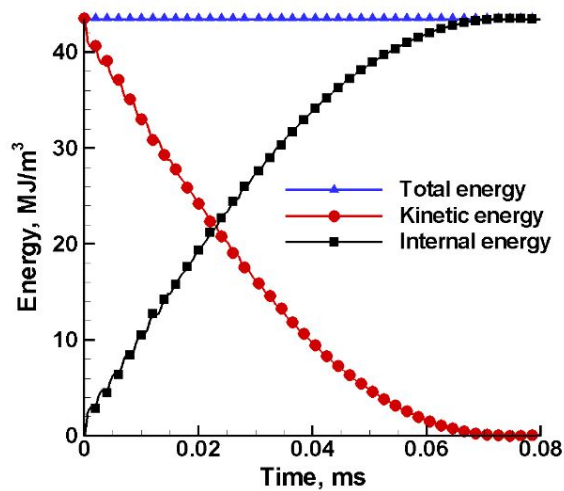


Fig. 4.8. Histories of the values of total, kinetic, and internal energy density under Taylor impact

Figure 4.8 shows the histories of kinetic, internal, and total energy densities, and indicates that the kinetic energy fully converts into internal energy under total energy conservation condition. The deformation stops approximately 80 μs after the impact of rod and rigid wall. Table 4.3 and Fig. 4.9 show comparison between experimental data and numerical results using changes of length, bottom radius and deformed shape. In Table 4.3, the numerical errors are 6~10% at early time (at 33 μs). However, with time, the numerical results approach experimental data with which the errors are declined to 0.4~4%. Also deformation shape of rod is similar to the experiment at each time as shown in Fig. 4.9.

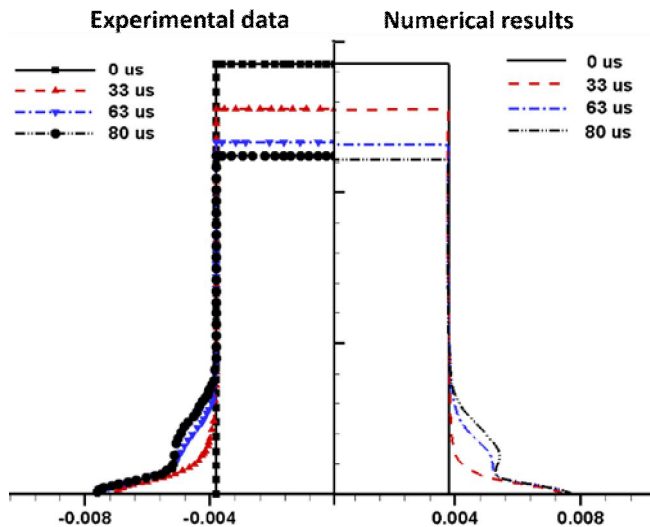


Fig. 4.9. Comparison between experimental data [39] and numerical results of copper rod shape

Table 4.3 Comparison between experimental data and simulation results

Time	Experiment [39]		Simulation	
	Length	Bottom radius	Length	Bottom radius
33 μ s	51.34 mm	7.02 mm	50.97 mm	7.44 mm
63 μ s	46.87 mm	7.68 mm	46.37 mm	7.70 mm
80 μ s	44.89 mm	7.68 mm	44.33 mm	7.70 mm

4.2.3. Multi-material problem

To deal with deformation of tube by gaseous detonation we need to consider multi-material interaction. So we perform a series of multi-material problems.

Firstly, we consider the stiff shock tube problem modeled by two different pressure and specific heat ratio considered in [34]. Equation (4.1) shows the initial conditions of each properties which show different pressure and specific heat ratio. Using HPLS method and GFM, we trace interface and determine the boundary values.

$$(\rho \quad u \quad p \quad \gamma) = \begin{cases} (1, 0, 500, 1.4) & x < 0.5 \\ (1, 0, 0.2, 1.667) & x > 0.5 \end{cases} \quad (4.1)$$

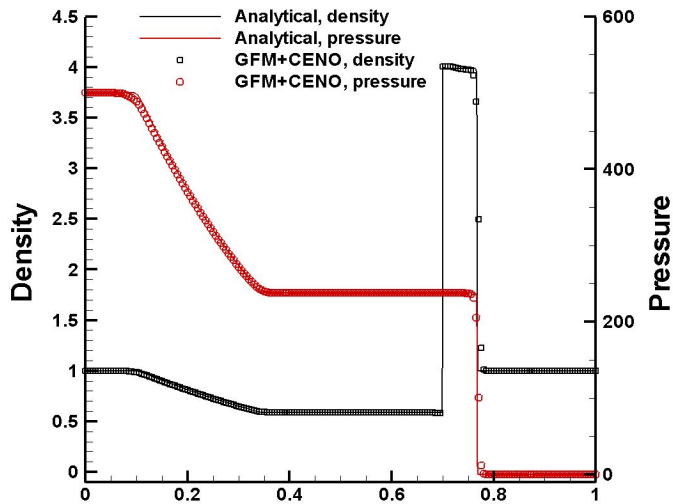


Fig. 4.10. Comparison between analytical [34] and numerical solution in Shock tube problems using Eq. (4.1)

Figure 4.10 shows the density and velocity profiles compared with exact solution at $t = 0.015$. In these figure, the shock front, material contact surface expansion pan are confirmed in profiles which are good agreement with exact solution. Additionally, we consider more different problem setup including different density, velocity, pressure, and specific heat ratio shown in Eq. (3.3). And this case indicates also good match with exact solution. (see Fig. 4.11).

$$(\rho \quad u \quad p \quad \gamma) = \begin{cases} (0.384, 27.077, 100, 1.667) & x < 0.6 \\ (100, 0, 1, 3.0) & x > 0.6 \end{cases} \quad (4.2)$$

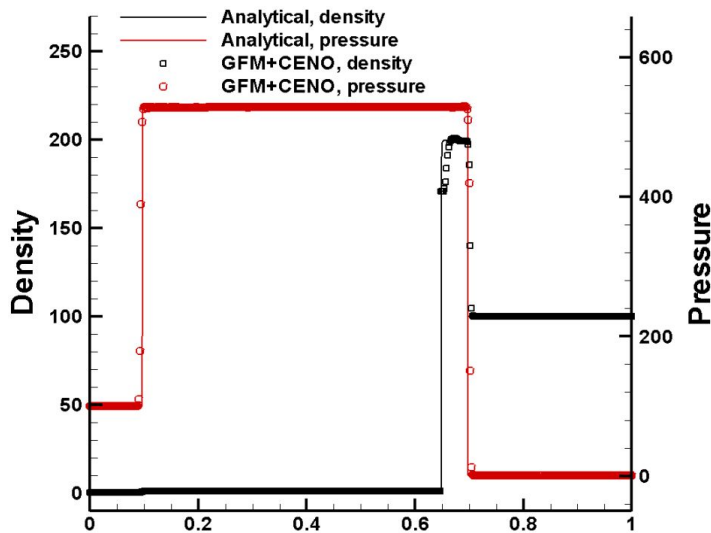


Fig. 4.11. Comparison between analytical [34] and numerical solution in Shock tube problems using Eq. (4.2)

As two-dimensional multi-material problem, the strong shock wave from an underwater explosion [40] interacts with a free surface, resulting in the bulk

cavitation near the free surface. The underwater explosion is a multi-material problem involving hot product gas interacting with cold water and water–ambient interface. Figure 4.12 shows the initial geometry of the underwater explosion problem.

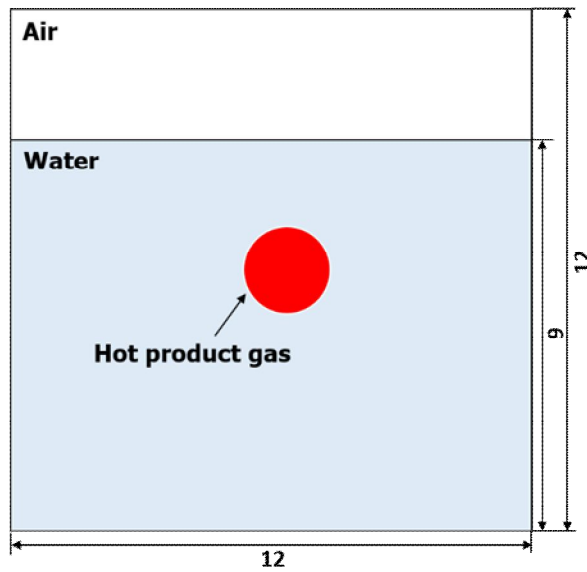


Fig. 4.12. Schematic of underwater explosion (unit: mm)

The normalized initial conditions are given as follows: a highly pressurized product gas of the unit radius is located at (6, 6) in water. The non-dimensional parameters of hot air bubble, ambient air, and water are like Table 4.4.

Table 4.4. Initial condition of hot air, ambient air, and water

Parameter	Hot air	Ambient air	Water
Density, ρ	1.27	0.0001	1
Pressure, P	8290	1	1000

The numerical result illustrated by pressure contours and interfaces is shown in Fig. 4.13. A shock wave generated in the center travels outward in water and makes contact with the free surface. The reflected wave and the transmitted wave occurred near the free surface are Prandtl–Meyer rarefaction wave and a relatively weak shock wave resulting from the big difference in impedance between water and air.

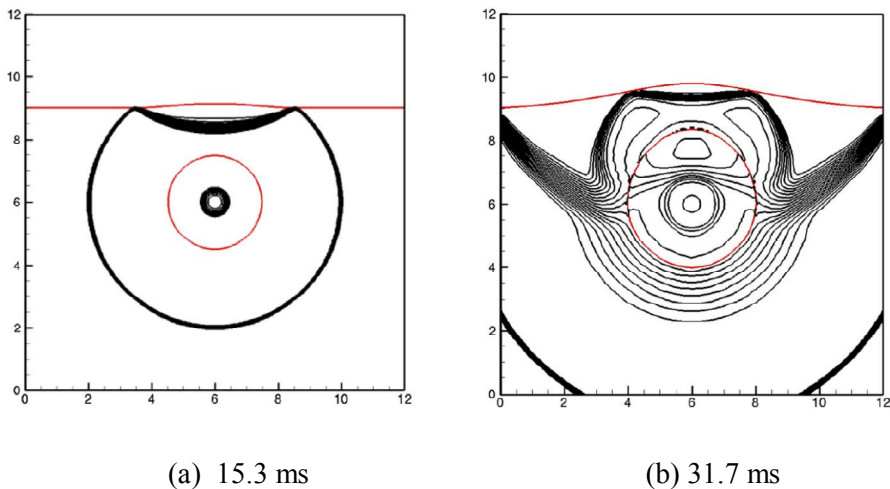


Fig. 4.13. Pressure contours and interfaces at 15.3 and 31.7 ms

Our numerical calculation is compared with the result of [41] in Fig. 4.14. The present calculation based on our HPLS algorithm reproduces the previously reported underwater explosion result.

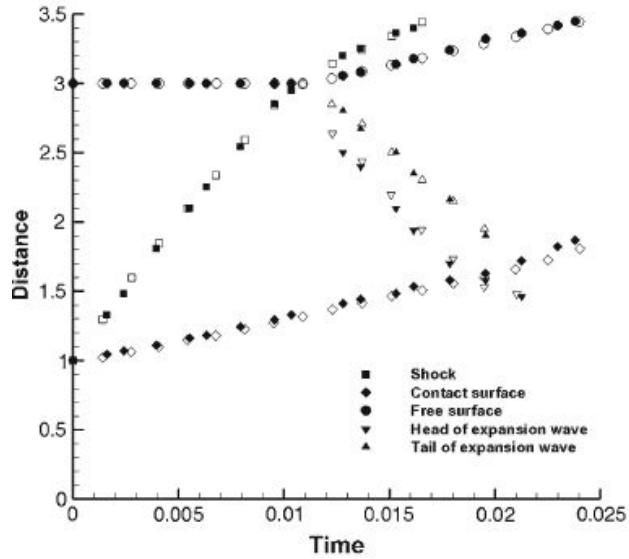


Fig. 4.14. Comparison between the Ref. [41] (hollow) and ours (filled symbols)

Next, we check the elasto-plastic deformation by detonation loading using residual plastic strain of a 304 SS tube under a $C_2H_4-O_2$ mixture detonation loading which is experimentally performed by Ref. [20]. In 2D cylindrical coordinate, kinetic mechanism of a $C_2H_4-O_2$ mixture is used with the Mie-Gruneisen EOS and the rate-dependent Johnson-Cook strength model for steel tube [42, 43]. The material properties and initial parameters for the $C_2H_4-O_2$ mixture and the steel are indicated in Tables 4.5 and 4.6, respectively. Figure 4.15 shows the setup of numerical calculation domain. The abnormal combustion of $C_2H_4-O_2$ mixture are considered Based on experiment setup of

Ref. [20] using 1D reactive compressible Euler equations with ‘tuned’ 1 step chemical reaction with ideal gas EOS.

Table 4.5. Initial condition and material properties of C₂H₄-O₂ mixture

Parameter	C ₂ H ₄ -O ₂ mixture
Initial density, ρ_0	1.268 kg/m ³
Initial pressure, P_0	1.003x10 ⁵ Pa
Initial temperature, T_0	295 K
Specific heat ratio, γ	1.232
Molecular weight, M_w	31x10 ⁻³ kg/mol
Pre-exponential factor, A	8x10 ⁸ m ³ /(kg s)
Activation energy, E_a	59035 J/mol
Chemical heat release, Q	4.597x10 ⁶ J/kg
C-J detonation pressure	32.6 P_0
C-J detonation velocity	2343 m/s

Table 4.6. Initial condition and material properties of steel (304 SS)

Parameter	Steel (304 Stainless steel) [42,43]
Initial density, ρ_0	7900 kg/m ³
Shear modulus, G	77.5 GPa
Yield stress, Y	110 MPa
Gruneisen coefficient, Γ_0	1.93
Normal sound speed, c_0	4570 m/s
S	1.49
Thermal conductivity, k	16.2 W/(m-K)
Poisson’s ratio, ν	0.29
Melting temperature, T_m	1694K

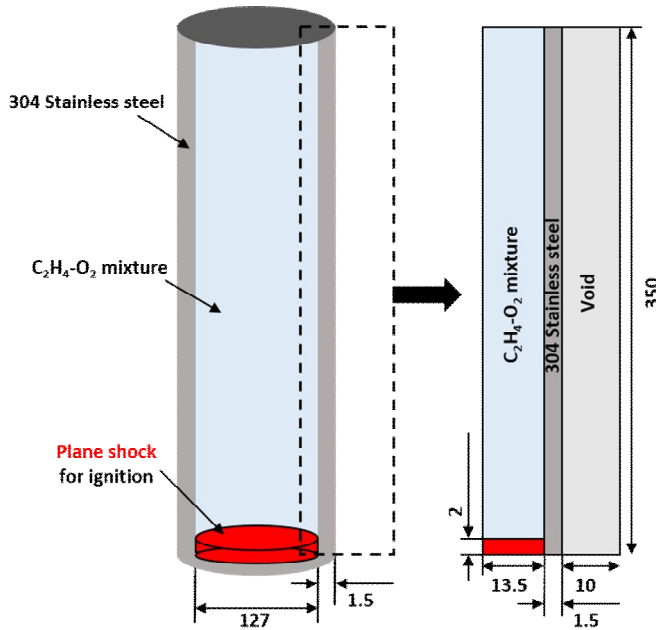


Fig. 4.15. Schematic of elasto-plastic deformation of steel tube by $C_2H_4-O_2$ mixture detonation (unit: mm)

Figure 4.16 shows pressure histories of the experiment and numerical result taken from the four gauges (P1, P2, P3, and P4) which are located at 1764, 1364, 964, and 0 mm from the end wall. In this figure, when detonation propagates toward the end wall, the pressure sharpens and the velocity reproduces to its experimental value. Whereas for the reflected shock waves, calculated pressure and velocity are higher than the experimental values. This is mainly due to neglecting the energy loss by friction and heat diffusion as well as turbulent mixing. While the numerical results are fairly descriptive of the measurements of Ref. [20], the chemical model is also quite reasonable for

depicting the state of detonation.

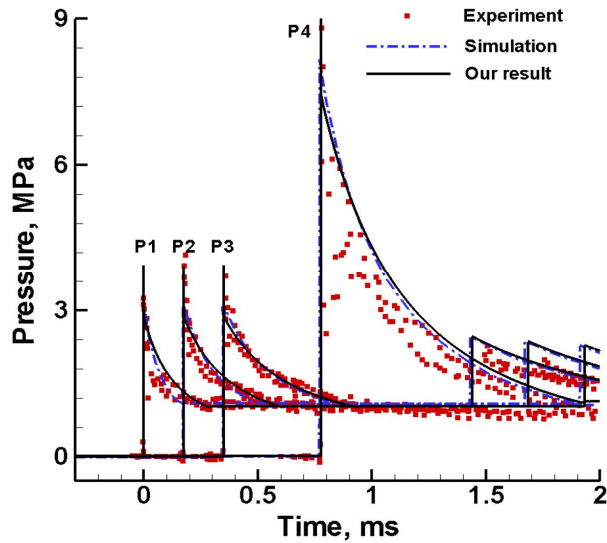


Fig. 4.16. Pressure history from experiment [20] and calculation of $C_2H_4-O_2$ mixture

And Fig. 4.17 shows the comparison of experimental [20] and calculated residual plastic strain under the 2 and 3 bar initial pressure conditions with a plastic strain distribution inside the tube. Here, numerical results are broader than experimental measurements moving away from the wall. This is because the model considers the liquefied solid phase right after the plastic deformation.

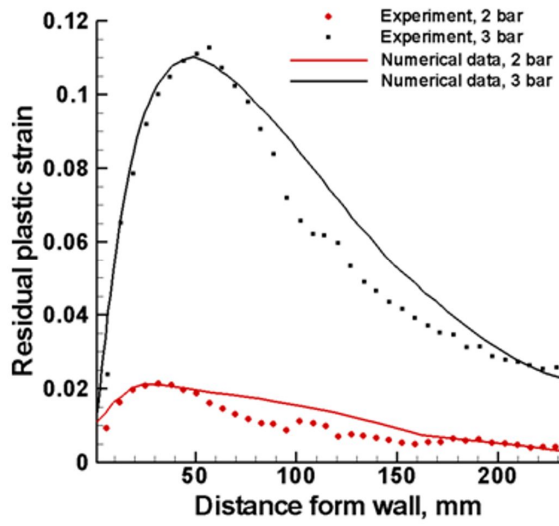


Fig. 4.17. Comparisons of experiment [20] and numerical results of residual plastic strain

4.2.4. Rigid tube

We simulate the detonation in a narrow tube of 2 mm inner radius and 0.2 mm thickness as a rigid tube. Figure 4.18 shows the snapshots of evolving density field. Here, the detonation propagates from the bottom with a velocity 2844 m/s. Then the reflected shock wave propagates from the top with a velocity 2000 m/s (see Fig. 4.18 (c)).

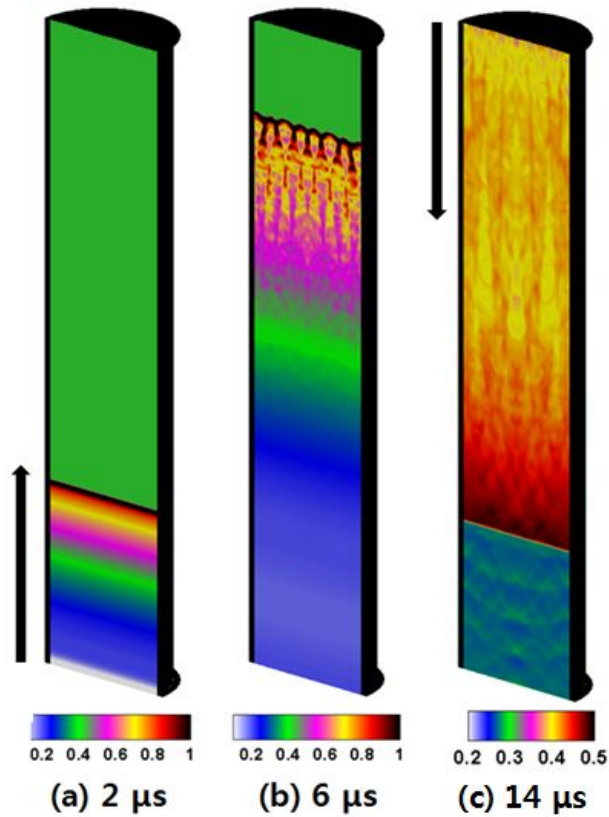


Fig. 4.18. Snapshots of density [unit: kg/m^3] in a rigid tube. Arrows indicate the propagation direction

Figure 4.19 shows the pressure profiles in 1D and 2D cylindrical coordinates. The velocities of detonation and reflected shock wave in 2D are identical to 1D ideal model. In the presence of a perturbation at the flame front by the thermal instability of detonation, however, complex unstable structure develops in the propagation direction, as the maximum pressure fluctuates and the pressure becomes higher than the von Neumann spike (3.38 MPa) of a plane detonation. Here we can also find out that the detonation velocity, CJ pressure, and maximum reflected shock wave pressure are 2844 m/s, 1.89 MPa, and 5 MPa ($P_{ref}/P_{CJ}= 2.6$), respectively.

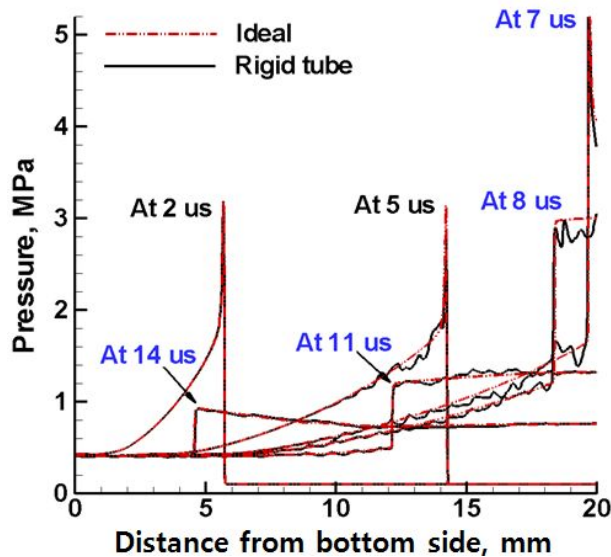


Fig.4.19. Pressure histories of an ideal (1D model) and rigid tube (2D cylindrical model)

4.2.5. Thin-walled tube

Contrary to the rigid tube result, the thin-walled tube is a deformable one under the high pressure loading by a detonation pressure. The thin tubes of 2 mm inner radius and 0.12 and 0.16 mm thickness are subjected to the same intensity of the aforementioned detonation loadings.

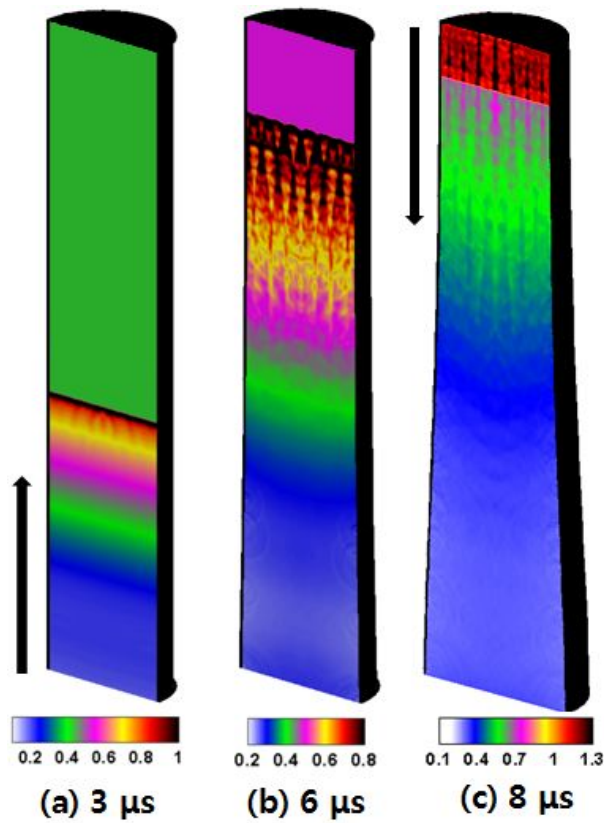


Fig. 4.20. Snapshots of density [unit: kg/m^3] in the thin-walled tube (0.12 mm thickness tube)

Figure 4.20 shows the density field of a 0.12 mm thickness tube. When the effective plastic stress exceeds the tube yield stress, the tube expands outwards and the expansion waves propagate toward the combustible gas (see Fig. 4.20(b) and (c)).

The expansion wave pressure is approximately 0.9 times the ambient detonation pressure. As the tube expands, multiple expansion waves are generated in the contact surface between the gas and the tube, as more complex flow field is constructed by the wave interactions. As a result, pressures and densities are decreased near the bottom side as compared to the rigid tube results.

For the case of a 2 mm inner radius and 0.16 mm thick narrow tube under detonation loading, a direct deformation does not occur; instead, the reflected shock wave whose maximum pressure (~ 5 MPa, $P_{ref}/P_{CJ}=2.6$) is higher than detonation pressure causes the tube to respond. Figure 4.21 shows snapshots of a density field in a 0.16 mm thickness narrow tube. Before deformation occurs by reflected shock waves, the flow field is identical to a rigid tube case. Once the reflected shock waves are generated and propagated, a sudden change in the flow field and the tube deformation occur (see Fig. 4.21 (b) and (c)). Near the top, the expansion of tube begins and multiple expansion waves are generated in the contact surface as similarly done in the bottom of a 0.12 mm thickness tube.

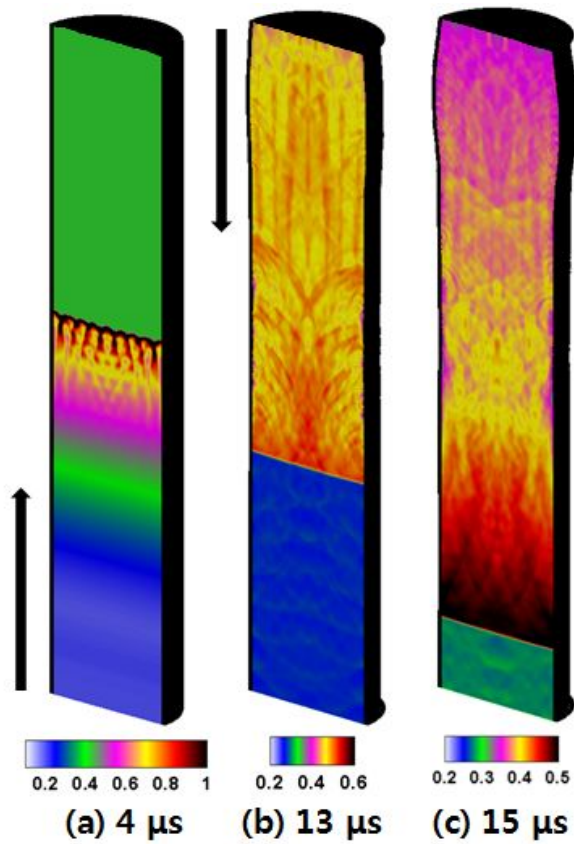


Fig. 4.21. Snapshots of density [unit: kg/m^3] in the thin-walled tube (0.16 mm thickness tube)

To confirm deformable wall effects such as the generation and superposition of the expansion waves, we performed simulation of tube deformation for different tube thicknesses under the same inner radius and detonation loading conditions. First, we compare the thin-walled tube of 0.12 mm thickness tube against a rigid tube.

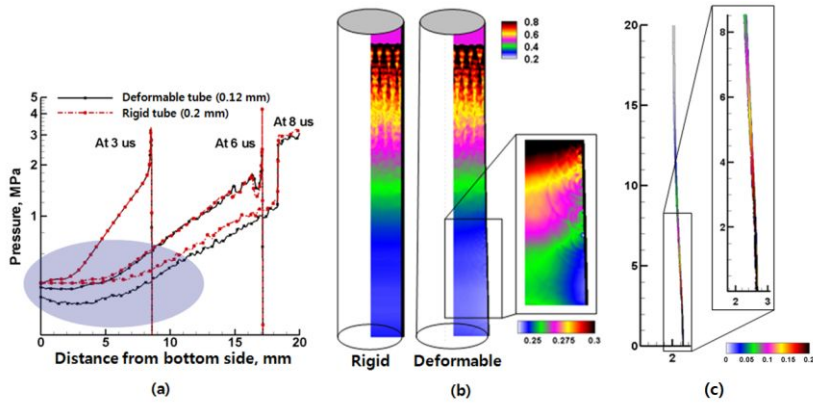


Fig. 4.22. Comparison between the rigid (0.2 mm thickness) and the thin-walled (0.12 mm thickness) tubes using (a) pressure histories, (b) density fields of each tube at 6.5 μ s, and (c) effective plastic strain fields in tube at 8 μ s

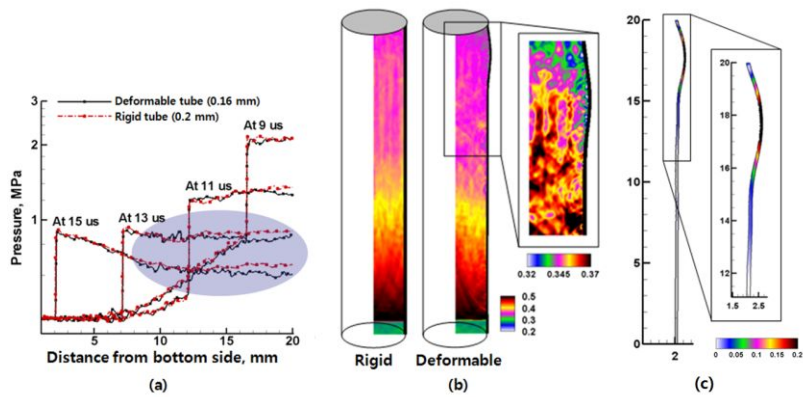


Fig. 4.23. Comparison between the rigid (0.2 mm thickness) and the thin-walled (0.16 mm thickness) tubes using (a) pressure histories, (b) density fields of each tube at 15.5 μ s, (c) effective plastic strain fields in tube at 17 μ s

In Fig. 4.22, flames propagate at the same velocity in both thin-walled and rigid tubes. The properties of the product gas are however noticeably changed upon tube deformation. The pressure of a rigid tube is approximately 0.4 MPa near the bottom at all times. However, in the case of the thin-walled tube with time, the pressure and density were decreased due to multiple generations of the expansion waves due to tube deformation that shows the increasing of effective plastic strain (see Fig. 4.22 (b) and (c)).

Figure 3.12 shows flame propagation details of small and large obstacle cases at $Ma=2.5$. In comparison, the formation of hot spots and direct initiation from these hot spots in each case are observed. In the small obstacle case, a hot spot did not directly initiate a detonation (see Fig. 3.12(a), (b)), due to insufficient reactants at a pressure of 0.9 MPa and at temperature of 600 K. In the large obstacle case, however, hot spot can initiate a direct detonation (see Fig. 3.12(c), (d)) because of a sufficiently high pressure of 1 MPa and temperature of 900 K. Hot spots of both cases are observed at nearly identical locations with similar intensity.

CHAPTER 5

REALISTIC WALL EFFECTS ON DETONATION

[44]

5.1 Numerical setup

The simulation objective is to investigate behaviors of detonation-loaded copper and steel tubes of varying wall thicknesses with the heated wall temperature conditions. Two-dimensional simulations of elsto-plastic deforming copper and 304 SS tubes exposed to the heated wall conditions are considered. The wall temperature is heated from the ambient temperature to 1000 K [45] as such the high temperature wall (above 873 K) may act as a catalyst during gaseous reaction [46]. Since copper and steel are inert materials, there is no affect in mixture reaction. However at such elevated wall temperature conditions, thermal softening plays a role that gives rise to a change in the metal properties and its thermal stresses. Four different wall temperatures ($T_w = 433$ K, 573 K, 773 K, and 973 K) are considered for investigating the heated wall effect on the resulting full dynamics of the considered tube loading problem. Also we deal with simulations of the disturbances of detonation field of combustible gas mixture induced by elastic vibration of 304 SS tubes. The considered tube thicknesses, t for copper tube

are 0.15, 0.2, 0.25, 0.3, 0.35, 0.4 and 0.45 mm. As for steel tube, they are 0.05, 0.08, and 0.12mm. All tubes have the same inner radius $r_i = 2$ mm. The two-dimensional cylindrical domain is depicted in Fig. 5.1 with its cross section (4 mm by 30 mm) shown with a varying tube thickness, t . The boundary conditions on the left, right, top, and bottom are symmetric, zero gradient, zero gradient, and extrapolated $Y_{boundary} = 0.95Y_I + 0.05Y_0$, respectively. For initiating a detonation, the CJ values initialize the bottom condition.

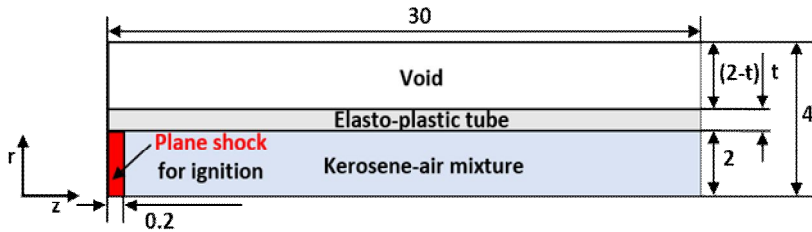


Fig. 5.1. Schematic of kerosene-air mixture detonation in elasto-plastic tube
(unit: mm)

5.2 Results and discussion

5.2.1. Validation and grid resolution test

We consider the detonation of kerosene-air mixture utilizing initial conditions and material parameters are listed in Table 5.1 using 1D/2D reactive compressible Euler equations with ‘tuned’ 1 step chemical reaction with ideal gas EOS.

Table 5.1. Initial condition and material properties of kerosene-air mixture

Parameter	Kerosene-air mixture
Initial density, ρ_0	1.236 kg/m ³
Initial pressure, P_0	1.01x10 ⁵ Pa
Initial temperature, T_0	433 K
Specific heat ratio, γ	1.33
Molecular weight, M_w	0.03036 kg/mol
Pre-exponential factor, A	8.0x10 ⁸ m ³ /(kg-s)
Activation energy, E_a	71036 J/mol
Chemical heat release, Q	1.9x10 ⁶ J/kg
C-J detonation pressure	18 P_0
C-J detonation velocity	1780 m/s

To assure numerical accuracy during simulation of the kerosene-air detonation, the mesh refinement is conducted. Figure 5.2 shows pressure profiles of three different mesh sizes 1/15, 1/50, and 1/100 mm for addressing the reaction zone refinement requirement. Both von Neumann spike and CJ pressure based on 1/50 and 1/100 mm resolutions are similar, and thus 1/50

(0.02) mm is chosen for all detonation calculations of kerosene-air mixture.

Figure 5.3 shows the pressure history together with temperature at $10 \mu\text{s}$ of the propagating detonation wave. The CJ pressure, 1.8 MPa and velocity, 1750 m/s are in agreement with the reference values [8, 46].

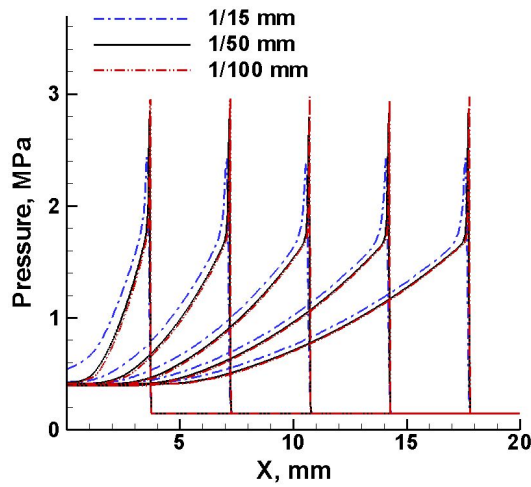


Fig. 5.2. Mesh resolution test for kerosene-air mixture detonation (1/15, 1/50, and 1/100 mm)

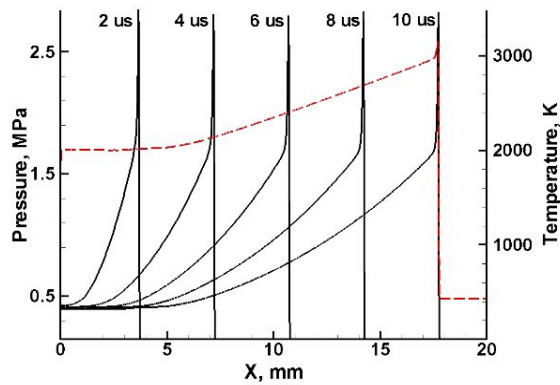


Fig. 5.3. Pressure history in solid line and temperature in dashed shown at
10 μ s

Following the Arrhenius rate law of detonation, two-dimensional cell structure of the kerosene-air mixture is sought. The domain is a tube of inner radius $r_i = 200$ mm as depicted in Fig. 5.4. The boundary conditions on top, bottom, right, and left are symmetric, wall, zero gradient, and extrapolated ($X_{boundary} = 0.95X_I + 0.05X_0$), respectively. Initially the CJ values are used to provide onset of detonation on the left. The numerically attained cell size of the kerosene-air mixture is validated against the experiment data [48]. Three different initial mixture pressures of 1, 1.5, and 2 bars are considered.

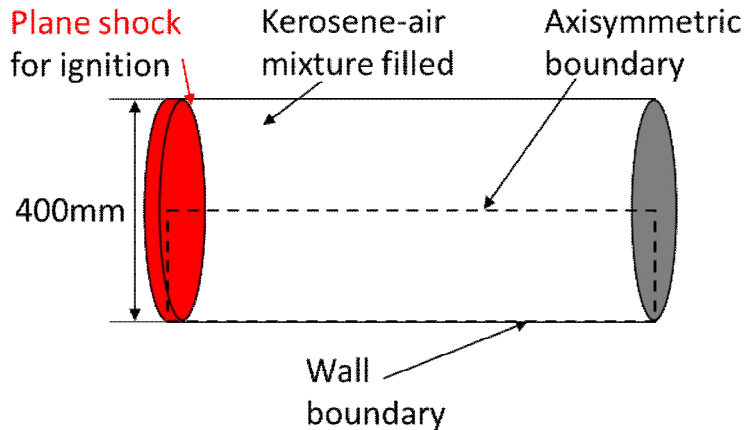


Fig. 5.4. Schematic of shock tube simulation for kerosene-air mixture
detonation at various initial gas pressures

The transverse wave formation gives rise to the unstable Mach stems as triple points appear in the two-dimensional detonation propagation. Shown in Fig. 5.5 is a shadowgraph image of the resulting cell size for 1 bar initial gas pressure shown at $15\mu\text{s}$. The cell width is approximately 40 mm, and the comparison between the experimental cell sizes for different pressure conditions is shown in Fig. 5.6. Higher initial gas pressure influences the CJ pressure, and thus triple point formation occurs sooner where the stronger incident shock and transverse waves leave the trace of narrower-width cells.

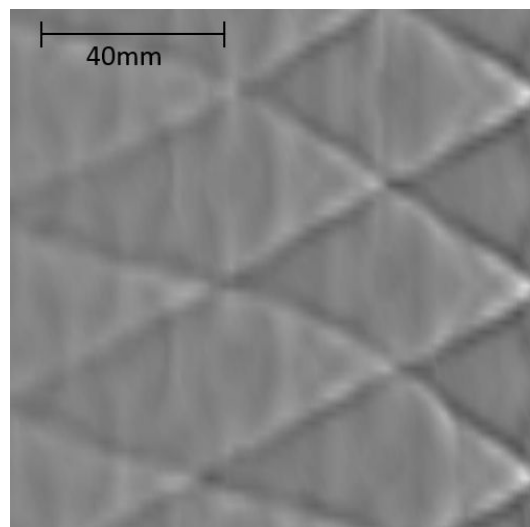


Fig. 5.5. Shadowgraph of calculated detonation cell structure of kerosene-air mixture at 1 bar initial pressure

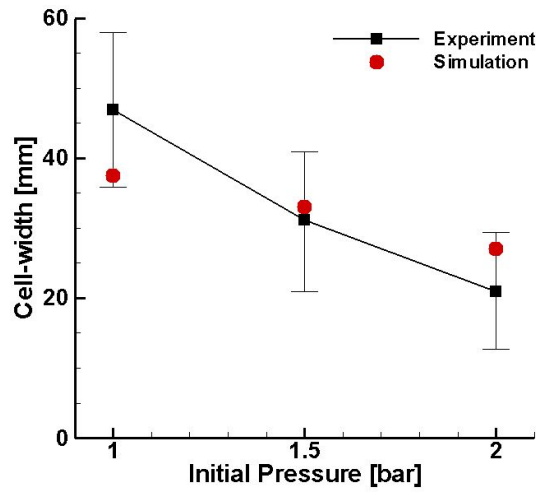


Fig. 5.6. Detonation cell width of kerosene-air mixture in comparison

5.2.2. Elastic response of metal

To confirm elastic response such as elastic vibration, we set 2D problem in rectangular coordinate, which is comprise of a rectangular plate, made of beryllium, with no a support and constraint in void. The plate is 60 mm X 10 mm located in calculation domain (70 mm X 30 mm) like Fig. 5.7. The centerline of the plate is located in 15 mm form the x-axis. The plate is prescribed with an initial y-axis velocity distribution as below Eq. (5.1) which is based on maximum velocity at center point and minimum at both edge points shown in Fig. 5.8.

$$u_y(x,y) = A \sin\left(\frac{x-0.025}{0.03} \pi\right) \text{ m/s} \quad (5.1)$$

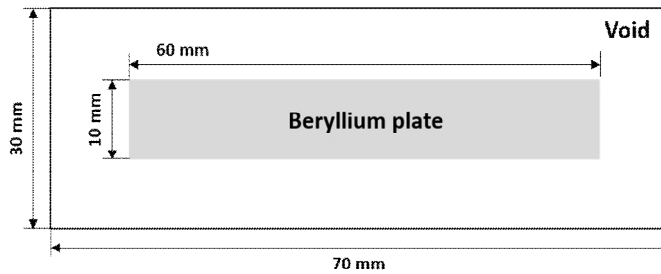


Fig. 5.7. Schematic of elastic vibration

Firstly, we check elastic vibration ($A=100$) of beryllium plate in void. The material properties and initial parameters for the beryllium plate are indicated in Table 5.2 We use very high yield strength value in order that the plate only

oscillates elastically.

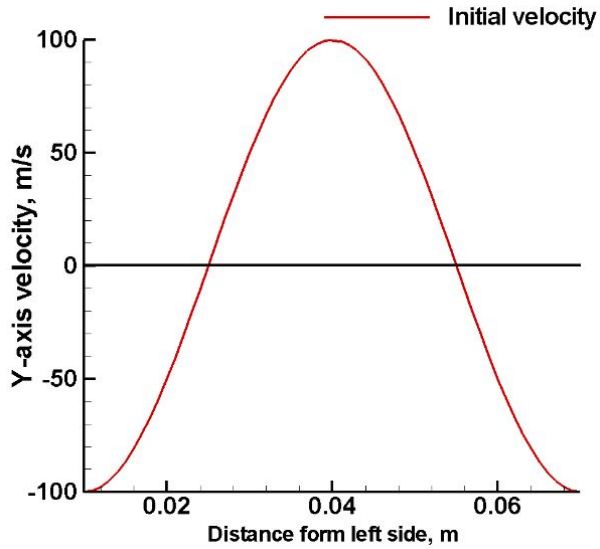


Fig. 5.8. Initial input (Y-axis velocity) condition ($A=100$)

Table 5.2. Initial condition and material properties of Beryllium

Parameter	Beryllium [48,49]
Initial density, ρ_0	8930 kg/m ³
Shear modulus, G	45 GPa
Yield stress, Y	90 MPa
Gruneisen coefficient, Γ_0	2.0
Normal sound speed, c_0	3940 m/s
S	1.49
Thermal conductivity, k	400 W/(m-K)
Poisson's ratio, ν	0.35
Melting temperature, T_m	1358 K

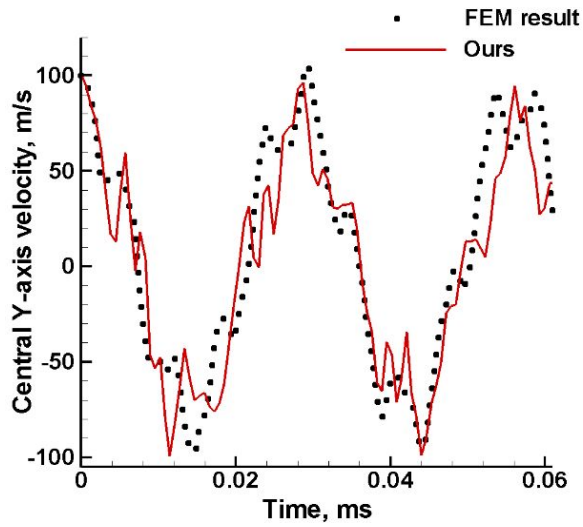


Fig. 5.9. Comparison between FEM result based on Ref. [50] and ours using history of y-axis velocity at center point

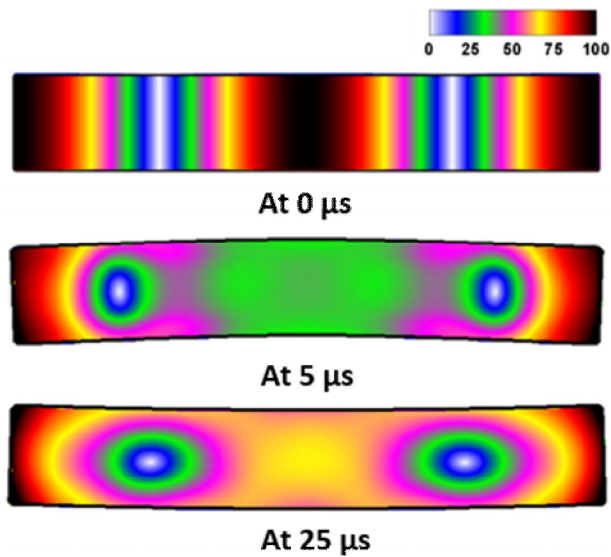


Fig. 5.10. Snapshots of velocity magnitude (unit: m/s) field inside of beryllium

In Fig. 5.9, frequency of y-axis velocity at center point which is calculated by the Eulerian approach shows approximately 33 kHz. And the result obtained by the normal mode analysis using MSC.NASTRAN (FEM result) shows 33198 Hz at the first bending mode [50]. The discrepancy between the frequencies predicted by the present analysis and FEM result shows below 3%. Thus, it is possible to conclude that the present structural model give a reasonable result. And Fig. 5.10 shows the beryllium plate behavior using velocity magnitude, $V (=u_x^2+u_y^2)$, which indicates the repeated elastic vibration.

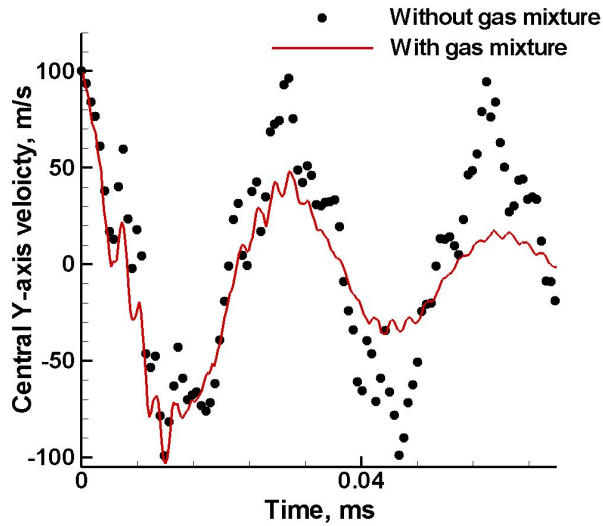


Fig. 5.11 Comparison between with and without gas mixture using y-axis velocity histories at center point

Additionally, we consider elastic vibration surrounded by high density gas mixture using multi-material interaction between beryllium plate and surrounded gas mixture. Figure 5.11 shows the central y-axis velocity histories of each only plate and the plate & gas mixture. Although the both frequencies are same value, the histories of velocity indicate that the elastic amplitude of plate in gas mixture is smeared by energy loss into the surroundings, contrast to result of the only plate. After approximately 0.25 ms, the amplitude of plate approaches to the zero like Fig. 5.12.

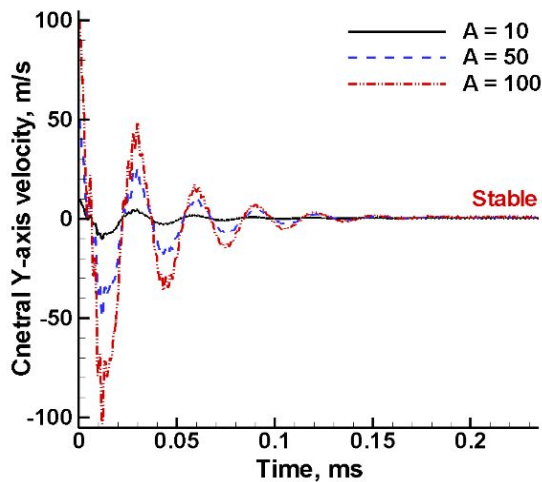


Fig. 5.12 Histories of y-axis velocity at center point in various initial velocity magnitude

Also we deal with lower initial amplitude condition ($A=10, 50$). In these

conditions, each frequency is nearly same to the existing amplitude condition ($A=100$). And the frequency is similar to Ref. [48] because the frequency is highly depended on material property and plate shape although the initial velocity profile is not identical each other.

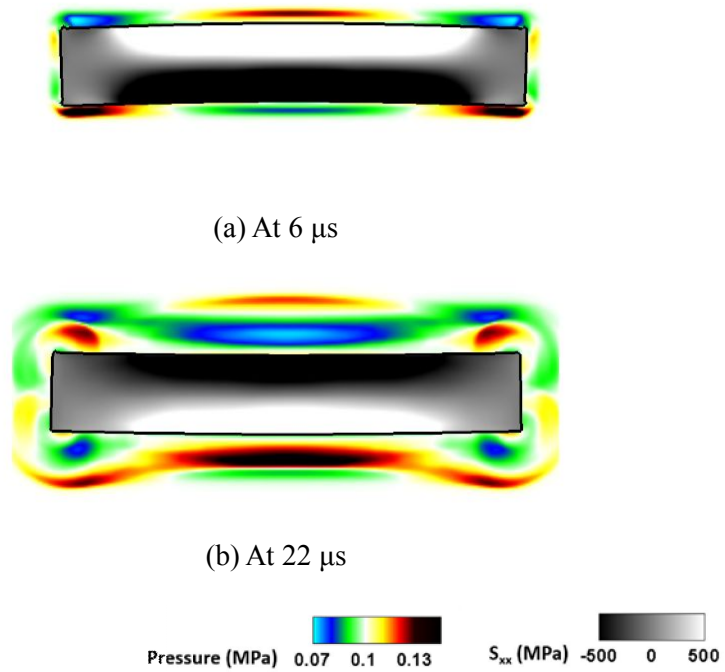
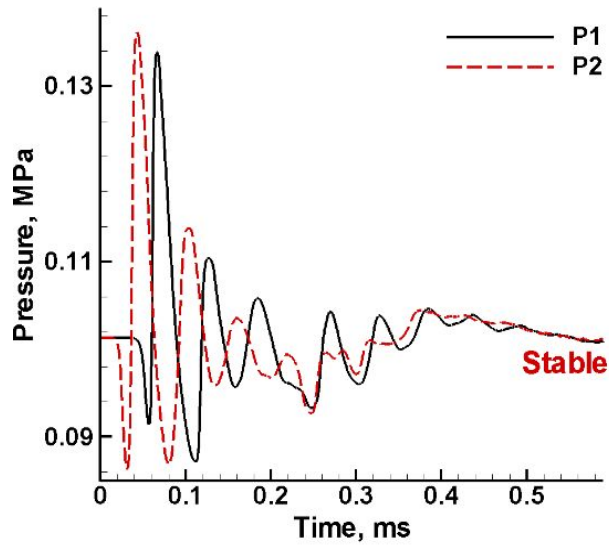


Fig. 5.13. Snapshots of deviatoric stress, S_{rr} field inside of plate and pressure field in gas mixture

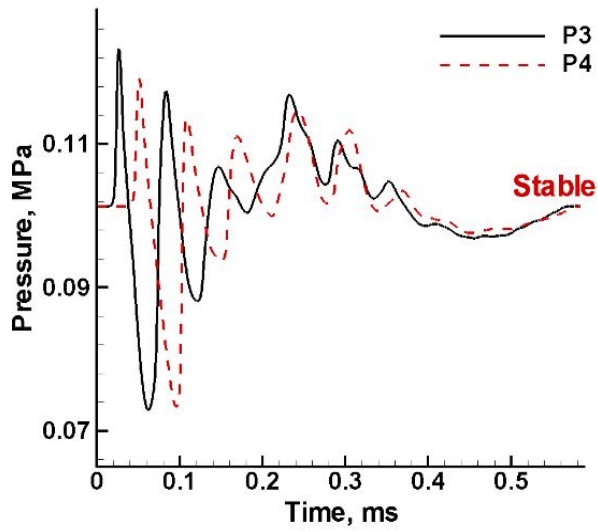
Next, to investigate the interaction of both materials, we check the deviatoric stress, S_{xx} of plate and pressure of gas mixture. Figure 5.13 (a) shows a snapshot of first bending of plate in the early state (at 10 μs). The

sign of deviatoric stress in underbody of plate is minors due to compression, whereas the sign of deviatoric stress in upper part of plate is plus by expansion. At the same time, in gas mixture below plate, the pressure decreases roughly 20 % compared to initial pressure, 0.1013 MPa because of expansion of gas mixture induced by rapidly compression of plate. And the drop of pressure leads the propagation of acoustic wave (expansion wave) to the opposite direction of plate. On the other hand, in gas mixture above plate, the pressure increases roughly 20 % owing to compression of gas mixture induced by fast expansion of plate. And the jump of pressure leads the propagation of acoustic wave (compression wave) to the other way of plate. As time passed, the stress distribution in the plate is reversed by the elastic behavior of plate (see Fig. 5.13 (b)).

In addition, it is observed that expansion (compression) changes compression (expansion) in gas mixture below (above) plate. This transition can be confirmed by time histories of numerical pressure gauges which are denoted in Fig. 6. The P1, P2, P3, and P4 are located in 3.3, 6.7, 23.3, and 26.6 from bottom side of calculation domain, respectively. Figure 5.14 shows pressure histories of gas mixture in the under (P1 and P2) and upper (P3 and P4) sections. In these Fig. 5.14 (a) and (b), the fluctuations of pressure are waned as time goes on, and the pressure go back to the stable pressure, 0.1013 MPa at 0.46 ms. The unstable time of gas mixture is longer than the vibration time of plate due to wave propagation in gas mixture.



(a) The lower section



(b) The upper section

Fig. 5.14. Pressure histories at numerical gauges P1, P2, P3, and P4 in gas mixture

5.2.3. Combined response of detonation loaded elasto-plastic tube

Steel has higher yield strength and melting temperature, thus 0.12 mm wall thickness is considered rigid even in the hot region. However copper tube can deform easily and such interesting observations are noted at high temperature cases. To point out the errors in making predictions on wall expansion when thermal softening is not considered, Fig. 5.15 is shown with the density for 0.2 and 0.15 mm thickness tubes under 433 K and 973 K wall conditions.

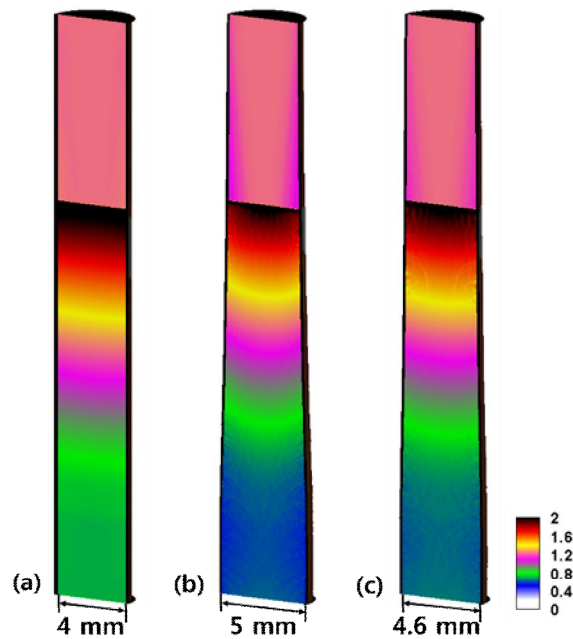


Fig. 5.15. Snapshots of density [unit: kg/m^3] in (a): $T_w=433\text{ K}$, $t=0.2\text{ mm}$, (b): $T_w=433\text{ K}$, $t=0.15\text{ mm}$, and (c) $T_w=973\text{ K}$, $t=0.15\text{ mm}$, all of which taken at $11.5\text{ }\mu\text{s}$ without thermal softening

There is no deformation for 0.2 mm case. As for 0.15 mm case for both cold and hot walls, the effective plastic stress exceeds the tube yield stress and thus the tube expansion is expected. The unreacted flow ahead of the detonation wave is affected by the tube expansion since the stress wave propagation within the solid is faster than a gaseous detonation velocity. The r-axis deviatoric stress, s_{rr} of the cold case (b) is approximately twice larger than the hot case (c) since the yield stress is inversely proportional to a temperature. Subsequently the expanding wall speed of cold case is approximately twice faster than the hot case of 973 K. This is rather unphysical, suggesting that one must include thermal softening in the analysis.

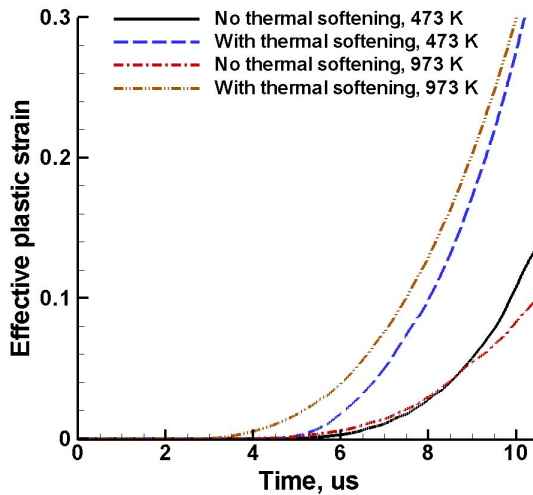


Fig. 5.16. Effect of thermal softening plotted with effective plastic strains at cold (433 K) and hot (973 K) wall temperature conditions

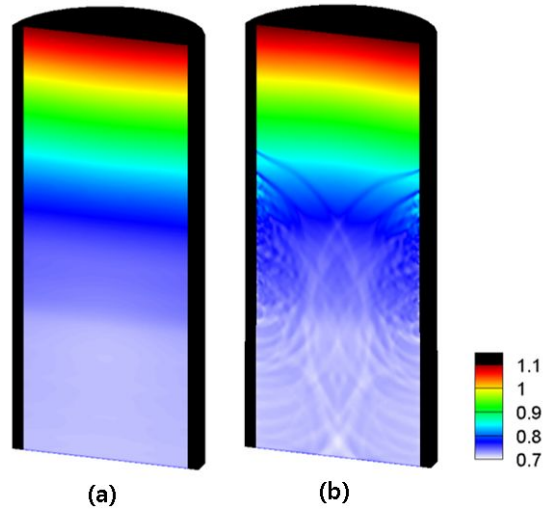


Fig. 5.17. Snapshots of density [unit: kg/m^3] in two cases of (a) no thermal softening and (b) with thermal softening under $T_w = 773 \text{ K}$ and $t = 0.25 \text{ mm}$ copper tube.

Now, with thermal softening included, the thermal stress states change readily, in particular with the rising temperature of the tube such that more wall expansion is expected for the higher temperature wall condition (see Fig. 7.17). In Fig. 5.17, the comparison between (a) without and (b) with thermal softening under the condition, $T_w = 773 \text{ K}$ and $t = 0.25 \text{ mm}$ copper tube using density fields is shown. And using impedance which is calculated as multiply density by sound speed and represents an acoustic wave intensity, Fig. 5.18 shows impedance fields in comparison between (a) without and (b) with thermal softening under same other conditions such as $T_w = 950 \text{ K}$ and $t = 0.1$

mm 304 SS tube. The tubes undergoes minute deformation with multiple expansion and compression waves that interfere with the internal detonation flow structure.

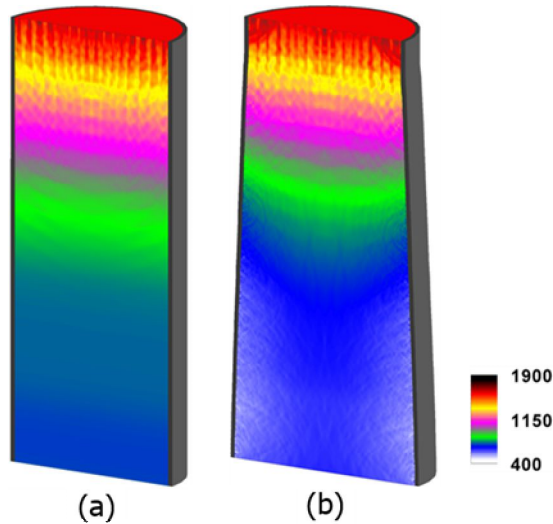
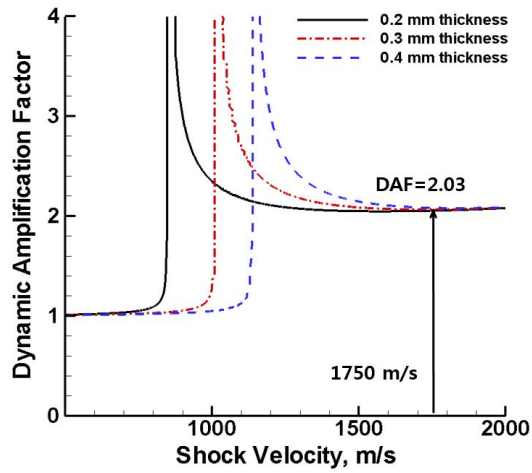


Fig. 5.18 Snapshots of impedance fields [unit: $\text{kg}/\text{m}^2\text{s}$] in comparison between (a) with thermal softening and (b) no thermal softening $T_w = 950 \text{ K}$ and $t = 0.1 \text{ mm}$ 304 SS tube

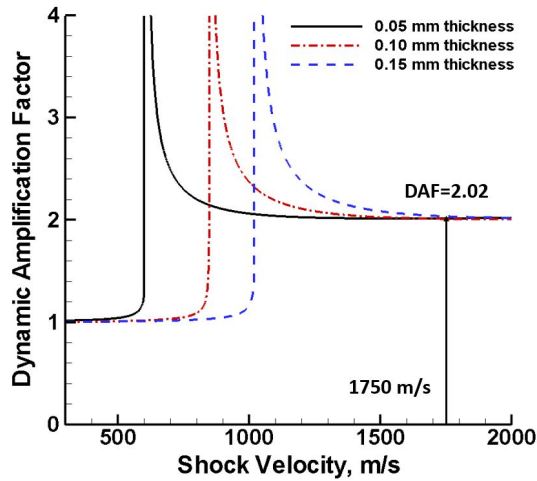
New we check theoretically critical thickness under high pressure loading. The theory on dynamic amplification factor (DAF), Φ and critical burst pressure, P_{burst} for plastic deformation of thin tube under detonation loading is considered. DAF is a ratio between the maximum dynamic strain $\epsilon_{dynamic,max}$ and the static strain ϵ_{static} [51]. The critical burst pressure could provide a

theoretical critical thickness of tube under kerosene mixture detonation loading, and the thickness is compared with the simulation result.

In Fig. 5.19, DAF for copper is 2.03, and it is 2.02 for 304 SS, which are obtained from the kerosene-air mixture detonation velocity of 1750 m/s.



(a)



(b)

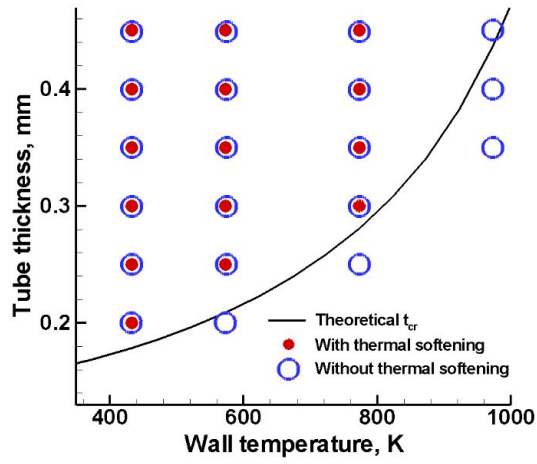
Fig. 5.19 DAF versus velocity of varying (a) copper and (b) 304 SS tubes thicknesses

As for the thin tube, the corresponding burst pressure [51] is given by the expression below:

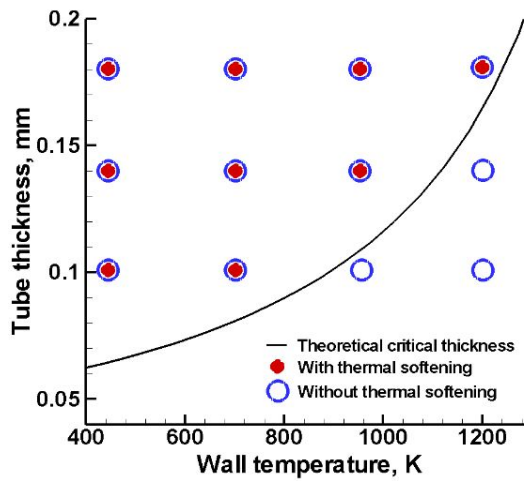
$$p_{burst} \approx \sigma_y \left[1 - \left(\frac{T - T_0}{T_m - T_0} \right)^{1.09} \right] \frac{t}{\Phi(r_i + t/2)} \quad (5.1)$$

where, T , T_m , T_0 , t , r_i , and σ_y are the wall temperature, the melting temperature, the reference temperature (293 K), the tube thickness, the inner radius, and yield stress, respectively. The above equation gives the approximated pressure upon the onset of a plastic deformation. The yield strength of copper tube changes by the thermal softening effect. From this equation, a critical thickness of copper and 304 SS tubes is determined from a burst pressure or the detonation pressure of kerosene-air mixture approximately 1.5 MPa

Figure 5.20 shows a safety or failure plot that describes the effect of thermal softening when it comes to providing the prediction of tube responses subjected to an internal detonation loading. The critical thickness from theory shown as a solid line is obtained from Eq. (5.1).



(a)



(b)

Fig. 5.20 The calculated (symbol) and theoretical (solid line) critical thickness plotted against heated wall temperature for (a) Copper and (b) Steel

5.2.4. Perturbed detonations in the elastic vibrating tube

In Fig. 5.1, the natural frequency of the tube is ~ 31 kHz (first longitudinal mode and second radial wave mode) calculated by the previous research [52] which presented the analytical natural frequency equations based on Rayleigh-method. So we simulate the detonation of kerosene-air mixture with very small elastic vibrating steel tube which has the frequency, 31 kHz and maximum strain, 0.00025.

Figure 5.21 shows numerical pressure histories of detonation in rigid and vibrating tubes at the central line.

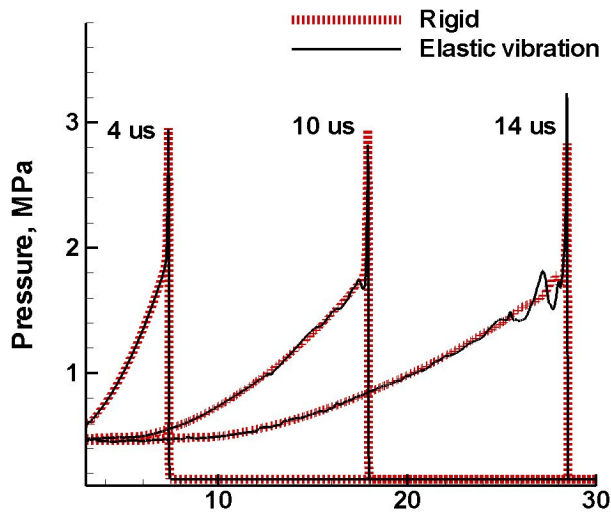


Fig. 5.21 Pressure profiles of detonation in rigid and elastic vibrating tubes

Although both pressure profiles in the early part (at $4 \mu\text{s}$) and detonation velocity (1750 m/s) are same, the pressure of detonation in vibrating tube is

more rapidly fluctuated than in rigid tube which can be perturbed by no-slip condition after relatively long time. In other words, the elastic vibration of tube can make the perturbations and disturb the detonation front, because the contact surface with gaseous mixture is changed as time goes on and it causes the r-axis small velocity (dr/dt) and pressure difference near the wall and develops the acoustic waves.

These phenomena can confirm with Fig. 5.22 which shows the density contour in rigid and elastic vibrating tubes at 8 μs and 14 μs . In the elastic vibrating tube, the flow field is disturbed from the tube and its effects represent the winding detonation front and acoustic waves in burned region.

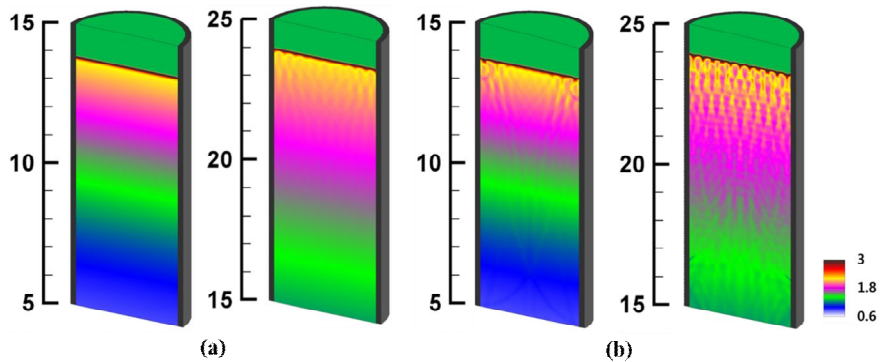


Fig. 5.22 Snapshots of density [unit: kg/m^3] at times 8 and 14 μs for (a) rigid wall and (b) elastic vibrating tubes

CHAPTER 8

CONCLUSION

Based on the unified approach, we deal with various numerical investigation relating to abnormal of combustible gas mixtures and elasto-plastic responses of containers (tubes) by detonation loading. Firstly, we confirm that the shock-flame interaction by the effects of complex confinement geometry (curved wall and obstacle) and initial flame size is critical for detonation transition of the shock-accelerated C_2H_4 -air flame. The simulations of straight tubes and bent tubes with obstacles show generation of the hot spots on walls or flame tips through multiple shock-flame interactions. Our simulations indicate that the multi-bends have advantage over the straight tube with obstacles in the detonation transition, and the initial flame size also plays a deciding role. Thus, flame propagation and DDT may be restrained or accelerated by the multi bend effects with obstacles and the initial flame size. Furthermore, when the chemical heat release rate averaged from the entire tube reaches above 20 MJ/(g·s), the first detonation transition is always observed. Such transition time is delayed due to the absence of reactant and insufficient pressure and temperature required for initiation. This suggests that instantaneous flame spread interrupts the initiation of detonation even though the hot spots are already formed. Our DDT study of hydrocarbon mixture on both geometrical conditions and initial flame size has strong potential for

enhancing the performance of a pulsed detonation engine (PDE) and providing counter measures that allow operators of nuclear power plants to avoid fatal flame accelerations or DDT.

Secondly, a careful evaluation of the wall boundary conditions and elasto-plastic deformation response of metal tubes of varying thicknesses and wall temperatures is performed in the context of multi-material high-strain rate phenomena involving detonative gas mixtures and their strong interaction with the tube. We confirm that calculated response of three different tube thicknesses under stoichiometric H_2-O_2 detonation loading using a high order multi-material. The present method that solves the continuum balance laws of detonation and plastically deforming boundary conditions is capable of predicting the dynamic response of a metal tube and the flow field of a detonative gas mixture subject to an internal detonation loading.

At last, in order to incorporate realistic tube response to a detonation tube, a unified simulation of the detonation flow and the responsive structures that vibrate elastically and deform thermo-plastically. Using the theory on DAF and burst pressure, also, the tube responses of copper and steel with different wall temperatures are considered. The reported predictions are in agreement with the pipe failure theory. We discover that thermal softening and elastic vibration of the tube must be considered when simulating the explosively pressurized tube by the kerosene-air detonation.

To acquire preliminary knowledge on interaction between (internal)

abnormal combustion and container which can be applied in design issues in propulsion systems and safety issues relating to explosion accidents, we conduct the various numerical investigations.

REFERENCES

[1] D. H. Kim, J. J. Yoh, "Predictive model of onset of pipe failure due to a detonation of hydrogen-air and hydrocarbon-air mixtures," *International Journal of Hydrogen Energy*, Vol. 34, pp. 1613-1619, 2009

[2] E. R. Vaidogas, and V. Juocevicius, "Sustainable development and major industrial accidents: the beneficial role of risk oriented structural engineering," *Technological Economic Devevelopmentn of Economy*, Vol. 14(4), pp. 612-627, 2008

[3] G. D. Roy, S. M. Frolov, A. A. Borisov, and D. W. Netze, "Pulse Detonation Engine: Challenges, Current Status, and Future Perspective," *Progress in Energy and Combustion Science*, Vol. 30(6), pp. 545-672, 2004

[4] P. G. Harris, R. A. Stowe, R. C. Ripley, and S. M. Guzik, "Pulse Detonation Engine as a Ramjet Replacement," *Journal of Propulsion and Power*, Vol. 22(2), pp. 462-473, 2006

[5] N. N. Smirnov and V. F. Nikitin, "Modeling and Simulation of Hydrogen Combustion in Engines," *International Journal of Hydrogen Energy*, Vol. 39(2), pp. 2025-2033, 2014

[6] M. Gwak, Y. H. Lee, K. H. Kim, and J. J. Yoh, "Deformable Wall Effects on the Detonation of Combustible gas Mixture in a Thin-walled Tube," *International Journal of Hydrogen Energy*, Vol. 40(7), pp. 3006-3014, 2015

[7] N. Tsubio, Y. Watanabe, T. Kojima, and A. K. Hayashi, "Numerical Estimation of the Thrust Performance on a Rotating Detonation Engine for a Hydrogen-Oxygen Mixture," *Proceedings of the Combustion Institute*, Vol. 35(2), pp. 2005-2013, 2015

[8] Y. Huang, H. Tang, J. Li, and C. Zhang, "Studies of DDT Enhancement Approaches for Kerosene-Fueled Small-Scale Pulse Detonation Engines Applications," *Shock Waves*, Vol. 22(6), pp. 615-625, 2012

[9] F. K. Lu and E. M. Braun, "Rotating Detonation Wave Propulsion: Experimental Challenges, Modeling, and Engine Concepts," *Journal of Propulsion and Power*, Vol. 30(5), pp. 1125-1142, 2014

[10] E. Dzieminska E, A. K. Hayashi, "Auto-ignition and DDT driven by shock wave-boundary layer interaction in oxyhydrogen mixture," *International Journal of Hydrogen Energy*, Vol. 38, pp. 4185-4193, 2013

[11] E. S. Oran, V. N. Gamezo, "Origins of the deflagration-to-detonation transition in gas-phase combustion," *Combustion and Flame*, Vol. 148, pp. 4-47, 2007

[12] G. Ciccarelli and S. Dorofeev, "Flame acceleration and transition to detonation in ducts," *Progress Energy Combustion Science*, Vol. 34, pp.199-550, 2008

[13] M. A. Liberman, M. F. Ivanov, A. D. Kiverin, M. S. Kuznetsov, A. A. Chukalovsky, and T. V. Rakhimova, "Deflagration-to-detonation transition in highly reactive combustible mixtures," *Acta Astronaut*, Vol. 67, pp. 688-701,

2010

[14] Y. Zel'dovich, "Regime classification of exothermic reaction with nonuniform initial condition," *Combustion and Flame*, Vol. 39, pp. 211-215, 1980

[15] S. M. Frolov, V. S. Aksenov, I. O. Shamshin, "Shock wave and detonation propagation through U-bend tubes," *Proceeding Combustion Institute*, Vol. 31, pp. 2421-2429, 2007

[16] S. Otsuka, M. Suzuki, M. Yamamoto, "Numerical investigation on detonation wave through U-bend," *Journal of Thermal Science*, Vol. 19, pp. 540-544, 2010

[17] M. Gwak and J. J. Yoh, "Effect of multi-bend geometry on deflagration to detonation transition of a hydrocarbon-air mixture in tubes," *International Journal of Hydrogen Energy*, Vol. 38, pp. 11446-11457, 2013

[18] G. D. Roy, S. M. Frolov, and D. W. Netzer, "Pulse detonation propulsion: challenges, current status, and future perspective," *Progress of Energy Combustion*, Vol. 30, pp. 545-672, 2004

[19] T. Uruno, S. Maeda, and J. Kasahara, "Study on detonation wave attenuation through narrow tube for application to explosion safety and detonation engines," *51th AIAA Aerospace Sciences Meeting*, 7-10 January 2013, Texas

- [20] J. A. Karnesky, "Detonation induced strain in tubes," PhD thesis. California Institute of Technology, Pasadena, California. 2010
- [21] J. A. Karnesky, J. S. Damazo, K. Chow-Yew, A. Rusinek, and J. E. Shepherd, "Plastic deformation due to reflected detonation," *International Journal of Solids Structure*, Vol. 50, pp. 97-110, 2013
- [22] W. M. Beltman and J. E. Shepherd, "Linear elastic reponse of tubes to internal detonation loading," *Journal of Sound Vibration*, Vol. 252, pp. 617-655, 2002
- [23] A. Heidari, S. Ferraris, J. X. Wen, V. Tam, "Numerical simulation of large scale hydrogen detonation," *International Journal of Hydrogen Energy*, Vol. 36, pp. 2538-2544, 2011
- [24] L. B. Tran, and H. S. Udaykumar, "A particle-level set-based sharp interface cartesian grid method for impact, penetration, and void collapse," *Journal of Computational Physics*, Vol. 193, pp. 469-510, 2004
- [25] K. Kim and J. J. Yoh, "A particle level-set based eulerian method for multi-material detonation simulation of high explosive and metal confinements," *Proceeding Combustion Institute*, Vol 34, pp. 2025-2033, 2013
- [26] S. Schoch, N. Nikiforakis, and B. J. Lee, "The propagation of

detonation waves in non-ideal condensed-phase explosives confined by high sound-speed materials,” *Physics and Fluids*, Vol. 25, pp. 086102-28, 2013

[27] J. Ponthot, “Unified stress update algorithms for the numerical simulation of large deformation elasto-plastic and elasto-viscoplastic processes,” *International Journal of Plasticity*, 18, pp.91-126, 2002.

[28] Z. Zhang, and J. T. Chen, “The simulation of material behaviors in friction stir welding process by using rate-dependent constitutive model,” *Journal of Materials Science*, 43, pp.222–232, 2008.

[29] D. Adalsteinsson and J. A. Sethian, “A fast level set method for propagating interfaces,” *Journal of Computational Physics*, Vol. 118, pp.269-277, 1995.

[30] D. Adalsteinsson and J. A. Sethian, “The fast construction of extension velocities in level set methods,” *Journal of Computational Physics*, Vol. 148, pp. 2-22, 1999.

[31] S. Osher and C. W. Shu, “High-order essentially non-oscillatory schemes for Hamilton-Jacobi equations,” *SIAM Journal on Numerical Analysis*, Vol. 28, 907-922, 1991.

[32] D. Peng, B. Merriman, S. Osher, H. Zhao and M. Kang, “A PDE-Based Fast Local Level Set Method,” *Journal of Computational Physics*, Vol. 155, pp. 410-438, 1999.

[33] K. H. Kim, M. C. Gwak, and J. J. Yoh, “An Enhanced Particle

Reseeding Algorithm for the Hybrid Particle Level set Method in Compressible Flows,” *Journal of Scientific Computing*, Vol. 65(1) pp. 1-23, 2014

[34] X. Y. Hu and B. C. Khoo, “An interface interaction method for compressible multifluids,” *Journal of Computational Physics*, Vol. 198(1), pp. 35-64, 2004

[35] G. Thomas, R. Bambrey, and C. Brown, “Experimental observations of flame acceleration and transition to detonation following shock-flame interaction,” *Combustion Theory and Modeling*, Vol. 5, pp. 573-594, 2011

[36] G. Cael, H. D. Ng, B.R. Bates, N. Nikiforakis, and M. Short, “Numerical simulation of detonation structures using a thermodynamically consistent and fully conservative reactive flow model for multi-component computations,” *Proceeding of the Royal Society A*, Vol. 465, pp. 2135-2153, 2009

[37] A. Nebu, T. Inagaki, H. Kawaeda, T. Inhida, M. Kuznetsov, “Structural response of steel pipes induced by hydrogen-oxygen detonation,” SMiRT 19, Toronto, August 2007, Paper#J04/3

[38] H. Udaykumar, L. Tran, D. Belk, and K. Vanden, "An Eulerian method for computations of multi-material impact with ENO shock-capturing and sharp interface," *Journal of Computational Physics*, vol. 186, pp. 136-177, 2003

[39] J. W. House, B. Aref, J. C. Foster Jr. and P. P. Gillis, "Film data reduction from Taylor impact tests," *Journal of Stain Analysis*, vol. 34(5), pp. 337-345, 1999

[40] T. G. Liu, B. C. Khoo, K. S. Yeo, "The simulation of compressible multi-medium flow II. Applications to 2D underwater shock refraction," *Computational Fluids*, Vol. 30(3), pp. 315–337, 2001

[41] W. F. Ballhaus, and M. Holt, "Interaction between ocean surface and underwater spherical blast waves," *Physics and Fluids* Vol. 17(6), pp. 1068–1079, 1974

[42] S. Lee, F. Barthelat, J. W. Hutchinson, and H. D. Espinosa, "Dynamic failure fo metallic pyromidal truss core materials - experiments and modelling," *International Journal of Plasticity*, Vol. 22 pp. 2118-2145, 2006

[43] E. Vitall, and D. J. Benson, "Modelling localized failure with arbitrary largrangian eulerian methods," *Computation Mechanics*, Vol. 49, pp. 197-212, 2012

[44] Y. Lee, M. Gwak, and J. J. Yoh, "Numerical investigation of kerosene-based pulse detonation loading on the metal tubes," *Journal of Propulsion and Power*, accepted

[45] K. Wang, W. Fan, X. Zhu, Y. Yan, and Z. Gao, "Experimental Investigations on Effects of Wall-Temperature on Performance of a Pulse Detonation Rocket Engine," *Experimental Thermal and Fluid Science*, Vol. 48 (1), pp, 230-237, 2013

[46] Y. Saiki, and Y. Suzuki, "Effect of wall surface reaction on a methane-air premixed flame in narrow channels with different wall materials," *Proceedings of the Combustion Institute*, Vol. 34 (2), pp. 3395-3402, 2012

[47] H. Shen, G. Wang, K. Liu, and D. Zhang, "Numerical Simulation of Liquid-Fueled Detonations by an Eulerian-Lagrangian Model," *International Journal of Nonlinear Sciences and Numerical Simulation*, Vol. 13(2), pp. 177-188, 2012

[48] S. K. Sambasivan, M. J. Shashkov, and D. E. Burton, "A finite volume cell-centered Lagrangian hydrodynamics approach for solids in general unstructured grids," *International Journal for Numerical Methods in Fluids*, vol. 72, pp. 770-810, 2013

[49] I. S. Menshov, A. V. Mischenko, and A. A. Serejkin, "Numerical modeling of elastoplastic flows by the Godunov method on moving eulerian grids," *Mathematical Models and Computer Simulations*, vol. 6(2), pp. 127-141, 2014

[50] Reference manual, MSC. NASTRAN, Version r2, MSC. Software, 2012

[51] S. Tang, "Dynamic Response of a Tube under Moving Pressure," *Journal of the Engineering Mechanics Division*, Vol. 5, pp. 97-122, 1965

[52] A. Goldack, *8st International Conference on Structure Dynamics*, Leuven, Belgium, 04-06 July 2011, pp. 3575-3581

초 록

다양한 기체 혼합물 (에틸렌-공기 혼합물, 에틸렌-산소 혼합물, 수소-산소 혼합물, 케로신-공기 혼합물 등)의 비정상 연소 현상(연소폭 발천이와 데토네이션)과 데토네이션 하중에 의한 탄소성 금속(구리, 304 스테인레스 스틸 등) 용기의 거동을 수치적으로 확인하기 위하여, 기체 혼합물과 금속 각각의 해석과 더불어 다물질 해석에 대한 연구를 수행하였다. 이를 위하여 유한차분법(FDM)을 기반으로 하는 공간 차분은 3차 Convex ENO 기법으로, 시간 차분은 3차 Runge-Kutta (RK) 기법을 사용하였으며, 다물질의 경계면 추적과 경계값 결정은 각각 modified hybrid particle level-set (MPLS) 기법과 ghost fluid method (GFM)을 활용하였다. 가연성 기체 혼합물의 경우, 이상기체 상태방정식을 통해 압력을 구했으며, 금속의 경우, Mie-Gruneisen 상태방정식과 강성모델로써 Johnson-Cook 모델을 사용하여 압력 및 항복응력을 구하였다.

비정상 연소 현상을 해석하기 위한 수치적 접근법의 적절성을 확인하기 위해 실험값 및 이론값을 기반으로 에틸렌-공기 혼합물, 에틸렌-산소 혼합물, 수소-산소 혼합물, 그리고 케로신-공기 혼합물의 1단계 아레니우스 형태 화학 반응식의 변수 값을 결정하였으며, 이

를 사용하여 1차원 혹은 2차원 비정상 연소 현상을 해석하고 C-J 조건 및 데토네이션 셀 크기와 비교 검증하였다. 또한 금속의 탄소성 거동을 해석하기 위한 수치적 접근법의 적절성을 확인하기 위하여 금속의 탄성 거동과 소성 거동을 각각 탄성 텀립 문제와 테일러 충격 문제로 검증하였다. 마지막으로 다물질 해석의 적절성을 확인하기 위하여, 데토네이션 하중에 의한 관의 변형 문제를 실험 자료와 비교 검증하였다.

다양한 검증 문제들을 통해 확보된 수치적 접근법을 사용하여 우선, 복잡한 관의 형상과 초기 화염 크기에 따른 연소폭발천이 현상의 변화를 확인하였다. 이를 위하여 장애물이 있는 직선 관과 굽은 관 내에서 충격파에 의해 유도되는 에틸렌-공기 혼합물의 연소폭발천이 현상을 고려하였다. 해석 결과를 통하여 화염과 충격파의 상호 충돌에 의한 열점의 생성을 확인하였으며, 데토네이션으로의 발전에 있어서 관 내 장애물의 긍정적/부정적 역할을 확인하였다. 또한 초기 화염 크기에 따른 연소폭발천이 현상의 변화를 통하여 가해지는 충격파의 세기에 따른 최적의 초기 화염 크기를 정성적으로 확인하였다.

다음으로 탄소성 관 내 에틸렌-산소 혼합물과 수소-산소 혼합물의 데토네이션 전파에 의한 관의 탄소성 변형 현상과 관의 소성 변형

에 의한 내부 데토네이션 유동장의 섭동 현상을 확인하였다. 에틸렌-산소 혼합물의 데토네이션 하중에 의한 관의 탄소성 변형을 실제 실험에서의 변형과 비교하였으며, 수소-산소 혼합물의 데토네이션 하중에 의한 관의 변형과 더불어 관 변형에 의해 내부 유동장에 전파되는 팽창파를 확인하였다. 그리고 동일한 데토네이션 하중에서 관 두께에 따른 관의 변형/손상을 예측하기 위하여 다양한 두께의 관을 고려하였으며, 이를 이론적인 한계 두께를 통해 확인하였다.

마지막으로 보다 실제적인 데토네이션 관의 거동을 확인하기 위하여, 고온의 환경에서 고유진동수로 떨리고 있는 관 내 데토네이션 전파 현상을 모델링하였다. 즉, 떨리고 있는 고온의 탄소성 관 내 케로신-공기 혼합물의 데토네이션 전파에 의한 관의 열 탄소성 변형과 관의 열 탄소성 변형 혹은 탄성 떨림에 의해 유발되는 내부 데토네이션 유동장의 섭동 현상을 확인하였다. 고온의 탄소성 금속 해석 시, 기존의 탄소성 관 해석에 추가적으로 열유화 효과(열응력)를 고려하여 열응력 유무에 따른 수치적 한계 두께를 구했으며 이를 이론적 한계 두께와 비교하여, 고온의 탄소성 금속 변형을 해석할 때에 열유화 효과가 적용되어야 함을 확인하였다. 그리고 관이 탄성으로 떨리는 경우 관의 변형은 거의 발생하지 않으나, 내부 데토네이션 유동장으로 전파하는 음파에 의한 섭동 현상을 확인하였

다.

본 연구에서 활용된 수치적 접근법은 가연성 가스 혼합물의 비정상 연소 해석, 탄소성 금속 거동 해석, 그리고 다물질 해석에 활용될 수 있으며, 분진/가스관/고압용기/원자력 발전소 내 발생할 수 있는 비정상 연소와 관련된 폭발 사고 연구 분야 및 고온에서 운용되는 PDE의 성능 향상과 관련된 발사체 추진 연구 분야의 초석이 될 것이다.

주요어: 가연성 기체 혼합물, 비정상 연소, 연소폭발천이현상, 데토네이션, 탄소성 금속, 다물질 해석

학 번: 2007-20762